PHYSICAL REVIEW FLUIDS **5**, 073301 (2020)

# Collective effects in the sedimentation of particles in a viscoelastic fluid

William L. Murch[1] and Eric S. G. Shaqfeh[1,2,3,*]
[1]*Department of Chemical Engineering, Stanford University, Stanford, California 94305, USA*
[2]*Department of Mechanical Engineering, Stanford University, Stanford, California 94305, USA*
[3]*Institute for Computational & Mathematical Engineering, Stanford University, Stanford, California 94305, USA*

(Received 16 December 2019; accepted 11 June 2020; published 22 July 2020)

The sedimentation of a suspension of rigid spherical particles in a polymeric fluid is studied employing experiments and particle-resolved numerical simulations. It is shown that the settling process in a viscoelastic Boger fluid is time-dependent and inhomogeneous; both experiments and simulations exhibit the formation of particle-rich, fast-settling regions and particle-depleted regions with backflow. The settling process in a Newtonian fluid is investigated for comparison and is shown to be homogeneous, with velocity fluctuations that decay following random mixing. In the viscoelastic Boger fluid, the mean settling rate is higher than that measured in a similar Newtonian suspending fluid, and in our experiments, higher than that of a single particle settling in isolation. When a cross shear flow is imposed, the mean settling rate in the viscoelastic Boger fluid is drastically reduced; the magnitude of the reduction is greater than that measured for a single particle, suggesting that both fluid elasticity and the suspension's particle volume fraction have important effects.

DOI: 10.1103/PhysRevFluids.5.073301

## I. INTRODUCTION

Particle suspensions are ubiquitous across industrial processes and in many natural settings. Often, the particles are more dense than the suspending fluid and settle under the action of gravity. Engineering examples can be found in oilfield applications, industrial separations, and additive manufacturing. Much of our understanding of these systems involves suspensions of particles settling in a viscous, Newtonian suspending fluid. However, in many industrially relevant processes, the suspending fluid is non-Newtonian, and the motion of suspended particles can be significantly altered, as detailed in reviews by D'Avino and Maffettone [1] and Zenit and Feng [2]. A particular case of interest involves sedimentation in a polymeric suspending fluid, which exhibits fluid viscoelasticity. In this work, we study the effects of fluid elasticity and an imposed external shear flow on the settling motion of a suspension of rigid spherical particles.

In Newtonian fluids, the sedimentation of a suspension of particles has received significant attention, and reviews by Davis and Acrivos [3] and Guazzelli and Hinch [4] provide excellent summaries of the work to date. While much progress has been made in understanding these systems, many important questions remain. Generally, it is understood that a suspension of particles sedimenting under creeping flow conditions remains homogeneous and exhibits a hindered average settling velocity. This can be represented by a hindered settling function, $\langle U \rangle = U_s f(\phi)$, where $U_s$ is the Stokes' settling speed (for a single particle), $\phi$ is the particle volume fraction, and $f(\phi) \leqslant 1$. This hindered settling is understood to be primarily due to fluid backflow, as originally shown

---

[*] esgs@stanford.edu

by Batchelor [5]. Many hindered settling functions have been proposed, both from theory (for dilute suspensions) and from empirical correlations [3]. Although the suspensions are visually homogeneous, careful particle tracking and PIV experiments have revealed that significant velocity fluctuations about the mean are present at steady state and grow as $\phi^{1/3}$ up to $\phi \sim 0.3$, at which point the settling velocity fluctuations can be nearly 1.5 times the mean [4]. In this context, steady-state conditions describe the long-time behavior when the variance in the particle settling rate approaches a steady value and does not vary significantly over time. The factors that control the magnitude of the velocity fluctuations remains an open question [4].

In a polymeric suspending fluid, the sedimentation of a suspension of particles has been less explored but has been highlighted as an area that deserves further investigation [4]. A few experimental studies have shown that the sedimentation process can be unstable in non-Newtonian fluids, resulting in an inhomogeneous suspension structure during settling [6–9]. Allen *et al.* [6] qualitatively described a nonhomogeneous settling process that involved rising liquid pockets and falling particle-dense regions in strongly viscoelastic fluids; this behavior became more pronounced with increasing fluid shear thinning. Joseph *et al.* [10] studied the interaction of pairs and groups of particles in a variety of fluids, reporting attraction and aggregation of particles in strongly viscoelastic fluids. They suggested that for viscoelastic fluids, a large value of the elastic stress ratio coefficient $\psi_{1,0}/\eta_0$, where $\psi_{1,0}$ is the zero-shear first normal stress coefficient and $\eta_0$ is the zero-shear viscosity, is a sufficient condition for strong aggregation. Bobroff and Phillips [7] used NMR imaging to study the time-dependent sedimentation rate and microstructure of a suspension of particles settling in weakly viscoelastic shear thinning fluids, strongly viscoelastic shear thinning fluids, and Boger fluids. They found that the settling process in weakly non-Newtonian fluids (including the Boger fluid) was similar to the Newtonian behavior. However, in the more strongly viscoelastic fluids, a time-dependent settling rate with rapid settling at the beginning of the process was observed. Images of the suspension showed an inhomogeneous microstructure with long vertical columns of particles, alternating with regions of nearly pure fluid. This was observed in the strongly viscoelastic fluids at particle shear rates above and below the critical shear rates for the onset of shear thinning; thus, it was concluded that either shear thinning or elasticity could result in the inhomogeneous sedimentation structure. Daugan *et al.* [8] and Mora *et al.* [9] studied the settling of monodisperse suspensions of rigid spheres in shear thinning polymeric solutions with small normal stress differences. Both studies reported that an initially well-mixed suspension evolved over time to form vertical columns of fast-settling particles surrounded by vertical particle-depleted regions. This “streamer” formation resulted in an enhanced overall settling rate [8] with a mean particle settling velocity that could be higher than the terminal velocity of a single particle [9]. To summarize then, an unstable, inhomogeneous sedimentation process has been observed in both shear thinning fluids with memory and viscoelastic fluids, where in both cases the settling process is characterized by the formation of aggregates or columns of particles that settle quickly out of suspension.

Two theoretical analyses have been suggested for this structural concentration instability during sedimentation [11,12]. Both theories are valid for a dilute suspension of spherical particles in weakly viscoelastic fluids (assuming a second-order fluid model). Both theories consider the sedimentation instability to depend on a competition between the aggregation of particles in a viscoelastic fluid and a hydrodynamic dispersion that acts to keep the suspension homogeneous. However, the underlying mechanism for particle aggregation differs between the two theories. Phillips [11] assumed the aggregation could arise from direct particle-particle interactions, since the aggregation of a pair of particles initially settling side-by-side in a viscoelastic fluid is well known [1]. Alternatively, Vishnampet and Saintillan [12] proposed that the particle aggregation was a consequence of the lateral drift of particles due to the nonlinear coupling between the particle’s settling motion and a local fluid velocity disturbance arising from density fluctuations in the suspension. Indeed, the lateral drift of particles settling in the flow direction of a sheared elastic fluid has been explored theoretically by a number of researchers [12–14], and recently supported by numerical simulations [15], where it has been shown that particles will drift toward streamlines pointing in the direction of the settling motion. The theory of Vishnampet and Saintillan [12] then used a continuum approach to perform a linear stability analysis, showing that concentration fluctuations can grow as a result of the anisotropic mobility of settling particles as they drift toward regions of higher particle concentration. A similar framework was presented originally by Koch and Shaqfeh [16] and used by Saintillan *et al.* [17] to explain the structural concentration instability observed in spheroids and deformable particles, respectively.

Simulations of multiple particles settling in viscoelastic fluids have been conducted by a number of authors, as reviewed by Zenit and Feng [2]. Although many advances have been made in recent years, to date these simulations are generally limited to a maximum of $O(10)$ particles, typically in two dimensions [18–22]. In general, these 2D simulations show evidence of particle chaining in elastic fluids. Yu *et al.* [23] studied the settling of 20 circular particles in a variety of suspending fluids, including Newtonian, shear thinning with memory, Oldroyd-B, and shear thinning viscoelastic fluids. They observed definitive particle aggregation in the shear thinning viscoelastic fluid and suggested that elasticity of the fluid is critical for particle aggregation. Recently, simulations of 228 circular particles in a square box filled with either a Newtonian or Oldroyd-B fluid were performed by Decoene *et al.* [24]; however, no significant differences were observed between the two fluids. In three dimensions, Pan and Glowinski [25] studied the dynamics of up to three spheres settling in an Oldroyd-B fluid, and Goyal and Derksen [26] studied the sedimentation of up to eight particles in a FENE-CR liquid. Only recently have large-scale 3D simulations of $O(10)$–$O(100)$ particles in a viscoelastic fluid become feasible [27–30]. In the present work, we simulate over 100 spherical particles settling in three dimensions in a viscoelastic fluid to investigate the collective effects present during the sedimentation process.

Despite its industrial relevance, only a few authors have studied a suspension of particles settling in a cross sheared viscoelastic fluid. This is a representative model system in oilfield applications, e.g., for the transport of particles into vertical cracks in a hydraulic fracturing process or for the suspension of cuttings in drilling muds [31]. Indeed, many engineering applications involve a dynamically moving suspension of particles. Experiments by Tonmukayakul *et al.* [32] showed that the mean particle settling rate of a sheared suspension of particles at $\phi = 0.02$ in a Boger-like fluid could be hindered beyond that predicted by single particle simulations [33]. Experiments by Bazilevskii [34] for suspensions of particles at $\phi = 0.20$ in a shear thinning viscoelastic fluid showed that the concentration instability in quiescent conditions was suppressed upon application of an external shear flow, although the mean settling rate increased due to the fluid's shear thinning viscosity. Krishnan *et al.* [27] used cross shear of a suspension of sedimenting particles as a proof-of-concept for an immersed boundary (IB) method (which is utilized in the present work). It was reported that the mean settling rate of confined particles was significantly reduced at increasing volume fraction up to $\phi = 0.05$ (with 210 particles) in the presence of a cross shear flow. These pioneering studies present an intriguing but incomplete picture. Thus, the settling behavior of a suspension of particles in a cross sheared viscoelastic fluid will be investigated in the present work using both experiments and simulations.

This paper is organized as follows. In Sec. II, we give an overview of the problem under study. The experimental methods, including the test fluids, experimental setup, and experimental procedure, are described in Sec. III. The numerical implementation and setup are described in Sec. IV. Results from experiments are presented in Sec. V and from numerical simulations are presented in Sec. VI. These results are summarized and compared, and physical mechanisms are proposed, in Sec. VII. Conclusions and directions for future work are presented in Sec. VIII.

## II. PROBLEM FORMULATION

The aim of this study was (1) to identity the salient differences between the settling behavior of rigid, non-Brownian spherical particles in a Newtonian fluid and a viscoelastic Boger fluid; and (2) to evaluate the effect of a cross shear flow on the settling behavior of a suspension of particles in a viscoelastic Boger fluid. To do so, we use both particle-tracking experiments and large-scale, particle-resolved, fully 3D numerical simulations.

For a sedimenting particle, the characteristic scales of the problem typically involve the particle radius ($a$) as the characteristic length, the terminal speed of a single particle ($U$) as the characteristic velocity, and the time it takes to settle one particle radius ($t = a/U$) as the characteristic time. For a rigid spherical particle settling in an infinite Newtonian fluid in the limit of vanishing inertia, the settling speed is predicted by Stokes' law,

$$U_s = \frac{2}{9}\frac{(\rho_s - \rho_f)a^2 g}{\eta}, \tag{1}$$

where $\rho_s$ and $\rho_f$ are the densities of the sphere and the fluid, $g$ is the gravitational constant, and $\eta$ is the fluid viscosity. For a small particle immersed in a viscous fluid, the particle Reynolds number $\mathrm{Re}_p = 2a\rho_f U_s/\eta$ is vanishingly small. Initially, we use the Stokes settling speed as our characteristic velocity, and we define a Stokes' settling time as $t_s = a/U_s$. Once our experimental and numerical geometries are described, we will use the speed of a single particle settling in the direction of gravity in a given settling cell and given fluid as our characteristic velocity. In general, this value must be measured experimentally or simulated, as it is not known *a priori*.

In a viscoelastic fluid, we can define a sedimentation Weissenberg number relating the polymeric fluid's characteristic relaxation time with the timescale associated with the sphere's settling motion as $\Theta = \lambda U/(2a)$, where $\lambda$ is the fluid's relaxation time associated with the entropic relaxation of stretched polymer macromolecules, and $U$ may differ from $U_s$ due to the effect of fluid viscoelasticity. Later, when we introduce a cross shear flow, we define a shear Weissenberg number as $\mathrm{Wi} = \lambda\dot{\gamma}$, where $\dot{\gamma}$ is the shear rate. In this work, we wish to study the sedimentation of a suspension of rigid particles in elastic fluids, when the sedimentation and shear Weissenberg numbers nonzero and increase to O(1) values.

## III. EXPERIMENTAL METHODS

To study the settling behavior of a suspension of rigid, non-Brownian spherical particles experimentally, we use a particle tracking method that allows for direct measurement of individual particles' position and velocity. Three main criteria were used to guide the formulation of the test fluids and the selection of the particles, taking inspiration from the experimental design by Ham and Homsy [35] and Nicolai *et al.* [36]. First, a viscous fluid was chosen to maintain creeping flow conditions for the Newtonian fluid and low Reynolds number conditions for all experiments. Second, the particles were chosen to be large enough to be simply tracked with a camera and to render Brownian effects negligible. Third, the index of refraction of the particles and fluid were chosen to be closely matched such that only intentionally marked particles would be tracked. Last, because we want to isolate the effects of fluid viscoelasticity, the viscosity and density of the Newtonian and viscoelastic fluids were chosen to be sufficiently close, such that any difference in settling rates could be attributed to the effect of fluid viscoelasticity. The choice of test fluids and fluid rheology are described in Secs. III A and III B. The choice of particles and the particle tracking method are described in Secs. III C and III D. Based on the choices described below, the particle Reynolds number $\mathrm{Re}_p = 2a\rho_f U_s/\eta < 10^{-3}$ and the Péclet number $\mathrm{Pe} = 6\pi\eta a^2 U_s/kT > 10^{10}$ for all experiments.

### A. Test fluids

Two test fluids were used in this study to investigate the effect of fluid elasticity on the settling behavior of a suspension of particles. The first fluid was an aqueous polyacrylamide-based polymeric fluid. This fluid was designed as a model elastic or "Boger" fluid, meaning a fluid with high fluid elasticity and a minimally shear thinning viscosity [37–40]. To do so, a low concentration of high molecular weight polyacrylamide was mixed in a viscous corn syrup and glycerol solvent.

The second fluid was a viscous Newtonian fluid made with corn syrup, glycerol, and water. The fluids were formulated to have very similar densities and viscosities (within the range of relevant shear rates in our experiments), such that any differences in settling behavior could be directly attributable to the elasticity of the Boger fluid.

The formulation of the viscoelastic Boger fluid was similar to that used in a previous work [41]. The fluid contained 63.64 wt% corn syrup (Fisher Scientific), 27.27 wt% glycerol (Sigma-Aldrich, $\geqslant 99\%$), 0.18 wt% polyacrylamide (Sigma-Aldrich, $M_w \approx 5 \times 10^6$ g/mol), and 8.91 wt% deionized water. The density of the Boger fluid was $\rho_f = 1300.4\,\mathrm{kg/m^3}$ and the index of refraction at 22 °C was measured to be 1.45. The Newtonian fluid used the same corn syrup and glycerol solvent as that used for the Boger fluid, and water was added until the viscosity nearly matched the zero-shear viscosity of the Boger fluid. The final concentration of each component was 69.64 wt% corn syrup, 29.84 wt% glycerol, and 0.52 wt% deionized water. The density of the Newtonian fluid was $\rho_f = 1330.8\,\mathrm{kg/m^3}$. Both fluids were mixed over a period of at least one week on a rolling jar mixer to ensure homogeneity while avoiding high shear rates during mixing.

### B. Fluid rheology

The test fluids were characterized using a rotational rheometer (ARES-G2, TA Instruments) with a 25 mm diameter cone-and-plate geometry. The temperature was fixed at 22 °C. The steady shear viscosity (for both test fluids) and first normal stress difference (for the viscoelastic fluid) are shown in Fig. 1(a). Results from the transient stress relaxation of the first normal stress difference following a step-strain for the viscoelastic fluid are shown in Fig. 1(b). In Fig. 1(c), the complex viscosity of the viscoelastic fluid from a small amplitude oscillatory shear test is shown. The rheological fit of our polymeric fluids using the FENE-P constitutive model is also shown in Fig. 1, and the model parameters are summarized in Table I. The choice of the FENE-P constitutive model is addressed later in Sec. IV A. The methodology for fitting the FENE-P model to the rheological measurements is as follows. From the small amplitude oscillatory shear tests [Fig. 1(c)], estimates for the zero-shear viscosity, $\eta_0$, and solvent viscosity, $\eta_s$, were obtained by averaging the plateau values of the complex viscosity at low and high frequency regimes, respectively. The zero-shear viscosity is defined as $\eta_0 = \eta_s + \eta_p$, where $\eta_p$ is the polymer viscosity. The value for $\eta_0$ was confirmed from the steady shear data; for this test fluid, the Cox-Merz "rule" was observed. The solvent contribution to the viscosity, $\beta = \eta_s/\eta_0$, was then calculated. To estimate a characteristic polymer relaxation time, the decay in the primary normal stress [Fig. 1(b)] was fit to a single exponential curve at long times to characterize the fluid's longest relaxation time. The remaining fitting parameter, $L^2$, which represents the finite extensibility of the polymer [42,43], was fit by minimizing the error between the model and the steady-shear data for the viscosity and the first normal stress difference. From Fig. 1(a), we observe that the viscoelastic fluid does shear thin at shear rates above $\dot{\gamma} > 1\ \mathrm{s}^{-1}$ (a power law index fit above $\dot{\gamma} > 1\ \mathrm{s}^{-1}$ yields $n = 0.88$). We refer to it as a Boger fluid since the shear thinning is minimal for the shear rates relevant to the motion of a single settling particle ($\dot{\gamma}_s \sim U_s/(2a) \sim 0.5$) in our experiments. The elastic stress ratio coefficient, $\lim_{\dot{\gamma}\to 0} \psi_1(\dot{\gamma})/\eta(\dot{\gamma}) = \psi_{1,0}/\eta_0 = 2(1-\beta)\lambda$, is 1.5 s in the viscoelastic Boger fluid. A large elastic stress ratio coefficient (greater than 0.5 s) was implicated as a sufficient condition for particle aggregation during sedimentation in the work of Joseph *et al.* [10], suggesting that particle aggregation may play a role in the viscoelastic Boger fluid used in our work.

### C. Experimental setup

In our experiments, we study the sedimentation of a suspension of rigid spherical particles in a quiescent fluid and a cross sheared fluid. To do so, we used two experimental settling cells. The first was a five-sided transparent acrylic box, shown in Fig. 2(a). This static settling cell was used to study suspension sedimentation in a quiescent fluid. The box had inner dimensions of $L_x = l = 250$ mm, $L_y = W = 10$ mm, and $L_z = h = 150$ mm and a wall thickness of 3 mm. The second experimental

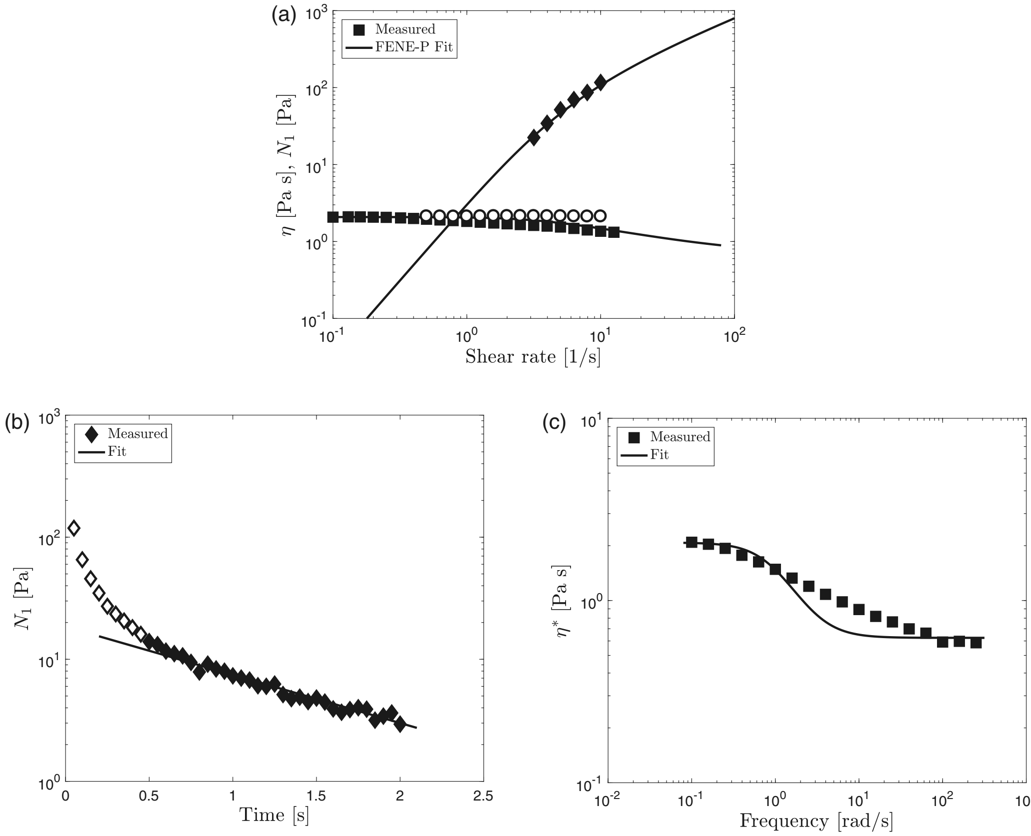

FIG. 1. Rheological measurements for the Boger and Newtonian fluids (*symbols*) and the FENE-P model fit (*lines*) from: (a) a steady-shear sweep, where closed symbols are for the viscoelastic Boger fluid (■, $\eta$; ◆, $N_1$) and open symbols are for the Newtonian fluid (○, $\eta$); (b) transient stress relaxation following a step strain (strain = 500%), where closed symbols (◆) are the fit data and open symbols (◇) are excluded from the fit; and (c) small amplitude oscillatory shear experiments, where closed symbols (■) are the fit data.

setup was a concentric cylinder apparatus (or Taylor-Couette flow cell), shown in Fig. 2(b). This apparatus, described previously [41], was used to apply a cross shear flow to a settling suspension. The inner cylinder had an outer radius of $R_i = 75$ mm and the outer cylinder had an inner radius $R_o = 85$ mm, for a gap size of $W = 10$ mm and a radius ratio of $\kappa = R_i/R_o = 0.88$. The height of the cylinders was $h = 150$ mm. Rotation of the cylinders were controlled via independently PC-operated motor drives (Compumotor CPHX106-220). The cylinders could be rotated independently and in either direction; in our experiments, we only use the counter-rotating setup to produce a cross shear flow. The volume between the two cylinders was filled with either the Newtonian or viscoelastic Boger fluid discussed in Sec. III B.

TABLE I. Fluid properties and FENE-P model parameters.

| Fluid | $\rho$ (kg/m$^3$) | $\eta_0$ (Pa s) | $\lambda$ (s) | $\beta$ | $L^2$ |
|---|---|---|---|---|---|
| Newtonian | 1330.8 | 2.13 | – | – | – |
| Viscoelastic | 1300.4 | 2.08 | 1.10 | 0.30 | 108 |

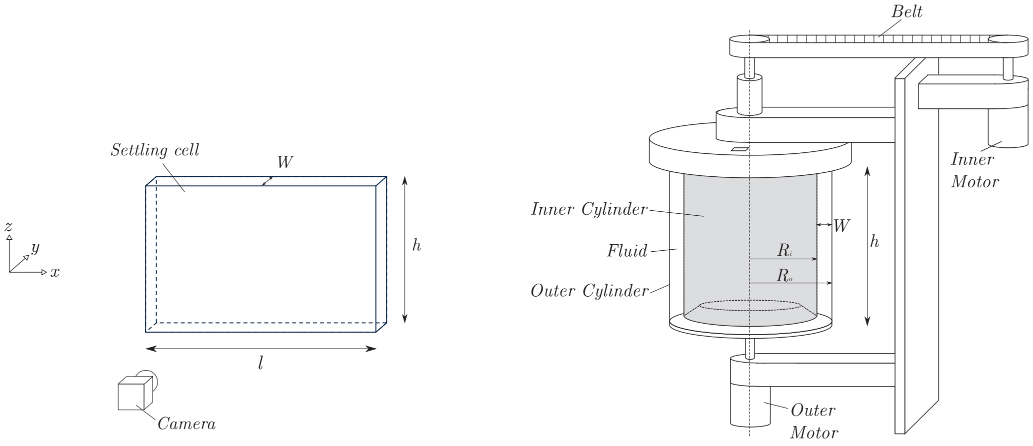

(a) Static settling cell

(b) Taylor-Couette flow cell

FIG. 2. Setups used for the suspension sedimentation experiments under (a) quiescent and (b) flowing conditions.

There were three main reasons why settling cells with a thin gap were chosen for this experimental study. First, we wanted to compare the settling dynamics under quiescent and cross sheared conditions, and a thin gap in a Taylor-Couette flow cell reduces the curvature of the shear flow velocity profile. Curvature in the shear flow velocity profile can give rise to particle migration [44], which could introduce a confounding effect into the experiments. Second, a thin gap allows for direct visualization of the settling dynamics including particle tracking, as done by Mora *et al.* [9]. Third, a thin gap (relative to particle size) is relevant to a number of applications, and particularly hydraulic fracturing, where suspensions of particles are transported into thin vertical fractures [31].

Neither the static settling cell nor the Taylor-Couette flow cell were temperature-controlled, so the temperature varied across all experiments by up to 1.5 °C. To account for this, the viscosity of both fluids were measured as a function of temperature within this range, and a viscosity-temperature relationship, $\eta = \eta(T)$ was fit. Results for the sedimentation velocity at a given $T = T_{\text{meas}}$ were adjusted to their assumed sedimentation velocity at $T_0 = 22\,^{\circ}\text{C}$ based on a Stokes' law correction, using the following expression: $U(T_0) = U(T)\eta(T)/\eta(T_0)$. We neglect the effects of any change in the Boger fluid's elastic properties in this small temperature range. It should be noted that no heat source—e.g., high temperature lights or laser sheet—were used in this setup. The fluid temperature was measured immediately prior to each experiment, and experiments were spaced sufficiently to allow for thermal equilibrium to be reached following an experiment. Thermal gradients were not detected in the settling cells when measuring the fluid temperature.

Both the static settling cell and the outer cylinder of the Taylor-Couette flow cell were made of transparent acrylic, allowing for video recording of the settling process. Acrylic has an index of refraction of approximately 1.49. The camera used for both experiments was a high resolution digital camera (Canon EOS Rebel T5i) with a CMOS sensor and a resolution of $1920 \times 1080$ px$^2$ recorded at 24 fps. An area of approximately $110 \times 62$ mm$^2$ at the center of the static settling cell was recorded during an experiment for a spacial resolution of 17 px/mm. In the Taylor-Couette flow cell, an area of approximately $160 \times 90$ mm$^2$ was recorded during an experiment for a spacial resolution of 8 px/mm. In both experimental setups, the camera was focused at the settling cell midplane.

The particles used in this study were spherical borosilicate glass beads ($\rho_s = 2230\,\text{kg/m}^3$) with a nominal diameter of $d = 1$ mm and a manufacturer's stated size tolerance of ±10% (Sigma-Aldrich). A sample of $N = 200$ spheres were measured using a micrometer, and the diameter was measured to be $d = \langle d \rangle \pm \sigma_d = 1.01 \pm 0.11$ mm, where $\langle \cdot \rangle$ denotes the arithmetic mean and $\sigma$ is the standard deviation. The distribution of sphere diameters from this sample are displayed in Fig. 4(a). Based on the thinnest settling cell dimension and the nominal sphere diameter, a confinement ratio can be defined as $\epsilon = d/W$ and $\epsilon = 0.1$ for all experiments. The glass beads had an index of refraction of approximately 1.52. To perform individual particle tracking and measurement of particle velocities, approximately 10% of the glass beads were coated with an enamel-based fluorescent green paint (Testors). The painted beads were sorted individually to ensure a uniform coating and to avoid aggregated spheres. A sample of $N = 100$ painted spheres were analyzed, and no significant difference in the mean particle diameter or particle density was measured (i.e., within measurement error).

### D. Experimental procedure

A typical experiment involved three main steps: (1) mixing of the suspension; (2) recording of the settling process; and (3) image analysis. For all experiments presented in this work, the volume fraction of the suspension was $\phi = 0.05$. First, the suspension was mixed inside the settling cell manually, using two laboratory spatulas. Manual mixing was done such that extra caution could be taken to avoid introducing air bubbles into the suspension at the air-liquid interface, although some air entrainment was unavoidable. In the Taylor-Couette flow cell, the mixing was done through the top of the device while the cylinders were rotating and applying a cross shear flow to aid the mixing process. In either setup, mixing was performed for several minutes until the suspension appeared visually homogeneous and no significant particle concentration gradients could be detected throughout the cell. After a short initial period ($t \approx 15t_s$), recording of the experiment began. The recording continued until the majority of the particles had exited the viewing window and the viewing window contained mostly particle-free supernatant fluid. Once the experiment was complete, the video was transferred to a PC for image analysis.

The image analysis was performed using the ImageJ/Fiji software package (v.2.0.0-rc-69, NIH) [45–47] with the TrackMate particle tracker plugin (v.3.6.0) [48]. In short, a raw image was processed to remove visual interference from unpainted spheres or small air bubbles in the fluid. Next, the Trackmate particle detection algorithm [48] was used to find the $x$ and $z$ location of the particle center-of-mass in pixels. This was then repeated for each frame, providing a data set of particle locations and trajectories. These particle locations and trajectories were then analyzed to calculate quantities such as the instantaneous particle velocity. Unless otherwise noted, particle velocities were calculated using a sampling period of $\Delta t = 1.25$ s ($\approx 0.6t_s$). From the particle velocities, quantities such as the mean and standard deviation of the settling velocity during an experiment were computed.

## IV. NUMERICAL SIMULATIONS

### A. Numerical implementation and boundary conditions

In our numerical simulations, we used an immersed boundary (IB) method, as presented by Krishnan *et al.* [27], to study the dynamic motion of suspended rigid particles. This method utilizes a fixed Eulerian mesh covering the entire computational domain, with particles represented by immersed Lagrangian meshes that are free to move inside the Eulerian mesh. The governing equations in dimensionless form over the Eulerian domain are

$$\frac{\partial u_i}{\partial x_i} = 0, \tag{2}$$

$$\mathrm{Re}\left(\frac{\partial u_i}{\partial t} + u_j \frac{\partial u_i}{\partial x_j}\right) = \frac{\partial \sigma_{ij}}{\partial x_j} + f_i, \tag{3}$$

where $f_i$ is a dimensionless forcing term that includes both the immersed boundary forcing $f_i^{\mathrm{IB}}$, which enforces rigid body motion of the suspended particles [27], and the forcing due to gravity $f_i^{\mathrm{grav}}$. The variables have been made dimensionless with a characteristic length ($2a$), characteristic velocity ($U$), and characteristic stress $[\eta_0 U_s/(2a)]$. The total fluid stress, $\sigma_{ij}$, can be written as a summation of the Newtonian and polymeric fluid stress,

$$\sigma_{ij} = -p\delta_{ij} + \beta\left(\frac{\partial u_i}{\partial x_j} + \frac{\partial u_j}{\partial x_i}\right) + \sigma^P_{ij}, \tag{4}$$

where $p$ is the fluid pressure, $\beta = \eta_s/\eta_0$ is the solvent contribution to the zero-shear viscosity, and $\sigma^P_{ij}$ is the polymeric fluid stress. To close this system of equations, we choose the finitely extensible nonlinear elastic constitutive model with Peterlin closure (the FENE-P model) to describe the polymer stress for the polymeric stress [42,43],

$$\sigma^P_{ij} = \frac{(1-\beta)}{\Theta}\left(\frac{c_{ij}}{1 - c_{kk}/L^2} - \delta_{ij}\right), \tag{5}$$

$$\frac{\partial c_{ij}}{\partial t} + u_k \frac{\partial c_{ij}}{\partial x_k} - c_{ik}\frac{\partial u_j}{\partial x_k} - c_{kj}\frac{\partial u_i}{\partial x_k} = -\frac{1}{\Theta}\left(\frac{c_{ij}}{1 - c_{kk}/L^2} - \delta_{ij}\right), \tag{6}$$

where $\Theta = \lambda U/(2a)$ is the sedimentation Weissenberg number, $c_{ij}$ is the dimensionless polymer conformation tensor, and $L$ is the dimensionless maximum polymer extensibility. Both $c_{ij}$ and $L^2$ are made dimensionless by scaling with the square of the equilibrium Hookean spring length. In the FENE-P model, an individual member of a dilute concentration of polymers is approximated as a single dumbbell connected with a finitely extensible nonlinear elastic spring. The polymer conformation tensor, $c_{ij}$, is defined as the configurationally averaged dyadic product of the polymer end-to-end vector, $c_{ij} = \langle R_i R_j \rangle$, where $R_i$ is the end-to-end orientation vector of the polymer dumbbell. Although a simplified molecular description, the FENE-P model captures the essential qualitative behavior of polymer chains in steady motion, as the modeled elastic dumbbells are both orientable and stretchable up to a finite extension [42,43]. Numerically, the FENE-P constitutive model is useful in scenarios with high rates of deformation, as the polymer conformation tensor and the polymer stress remain bounded [49,50]. For a single sphere, the FENE-P model has been shown to reasonably capture the qualitative behavior during sedimentation [51], even in the presence of an external flow with significant polymer stretching [i.e., at O(1) Weissenberg number] [41]. To enable the large-scale simulations of many particles, we employ a single-mode FENE-P model, and acknowledge that this model does not accurately describe the full spectrum of relaxation times of a polymeric fluid, as observed in Fig. 1. The implications of using this coarse-grained model will be discussed in Sec. VI.

In this work, we study the motion of a suspension of $N_p$ rigid spheres settling in a Newtonian or viscoelastic fluid due to gravity. These particles move as rigid bodies with velocities $u^n_i = U^n_i + \epsilon_{ijk}\Omega^n_j r^n_k$, where $r^n_k$ is the vector from the center of mass of particle $n$, with $n = 1, 2, \ldots, N_p$. The particle translational velocity, $U^n_i$, and angular velocity, $\Omega^n_j$, are calculated as part of the immersed boundary algorithm by conserving the linear and angular momentum of the fluid on the Eulerian mesh underlying each Lagrangian particle mesh using the immersed boundary force, $f^{\mathrm{IB}}_i$. The full description of this IB method, including the algorithm that is employed to solve for $f^{\mathrm{IB}}_i$, is described in detail by Krishnan *et al.* [27].

A schematic for the computational domain $D$ is shown in Fig. 3. For all simulations, the computational domain is of size $L_x = 40a$, $L_y = W = 20a$, and $L_z = 20a$. In all cases, the system begins from rest, with $u_i = 0$ and $c_{ij} = \delta_{ij}$. In the $x$ direction, the boundaries are periodic. In the y-direction, the boundaries are no-slip and no-penetration walls: during simulations of a static settling process, the velocity boundary condition on the walls are $u_i = (0, 0, 0)$ at $y = \pm W/2$. During simulations of a cross sheared settling process, the velocity boundary condition on the walls are $u_i = (\pm\dot{\gamma}W/2, 0, 0)$ at $y = \pm W/2$. In the z-direction, the boundaries are periodic. However, as discussed in Sec. I, the presence of fluid backflow in a suspension is critical to the suspension dynamics and must be taken into account. To model backflow within a periodic computational

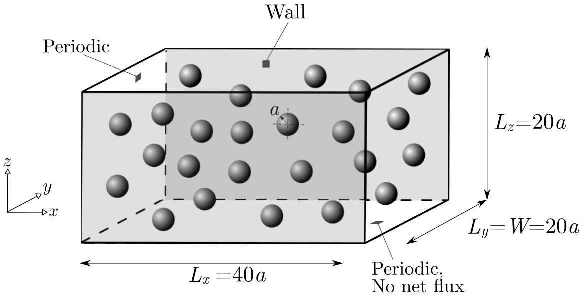

FIG. 3. Computational domain used for simulating suspensions of particles settling in a confined channel.

domain, the condition we wish to satisfy is a no net flux condition on the bottom boundary,

$$\int_{S_b} u_i n_i dS = 0, \tag{7}$$

where $S_b$ is the bottom boundary of the computation domain and $n_i$ is the normal vector on the bottom boundary. To achieve this, we use the following expression for the momentum source term due to gravity,

$$f_i^{\text{grav}} = \left(1 - \frac{\rho_{\text{eff}}}{\rho}\right) g_i, \tag{8}$$

where $\rho$ is the local density on the Eulerian grid and $\rho_{\text{eff}}$ is the effective density of the suspension. The local density $\rho$ can be defined in terms of an indicator function $\chi$, which defines the regions of the Eulerian mesh that underlie Lagrangian particle meshes,

$$\rho = \rho_s \chi + \rho_f (1 - \chi). \tag{9}$$

The indicator function is equal to one inside the particle regions and zero outside of the particle regions, and is smoothed continuously at the fluid-particle boundary such that $0 \leqslant \chi \leqslant 1$, where the length of this "smeared" region is of the order of the Eulerian mesh resolution [27]. At the beginning of the simulation, the effective density of the suspension $\rho_{\text{eff}}$ is equal to the volume averaged density. At each subsequent time step, $\rho_{\text{eff}}$ is updated explicitly subject to the constraint given in Eq. (7). In all simulations in this work, following a short transient period of approximately $t_s = a/U_s$, $\rho_{\text{eff}}$ deviates from the volume averaged density by less than 0.1%. Thus, for dense, settling particles, $f_i^{\text{grav}}$ is aligned with $g_i$ inside the particle regions ($\rho > \rho_{\text{eff}}$) and opposite $g_i$ in the fluid regions ($\rho \leqslant \rho_{\text{eff}}$), giving rise to fluid backflow. The height of the computational domain was chosen to be $L_z = 20a$, such that the time for a single, isolated particle to settle through the computational domain is approximately $20t_s$ and greater than $35\lambda$.

For the simulations, we set the same fluid parameters as discussed in Sec. III A and III B and shown in Table I. Similarly, the same sphere parameters as described in Sec. III were set in the simulations such that the net gravitational body force on the spheres in our simulations was the same as in the experiments. As in the experiments, the sphere sizes were sampled from a normal distribution of $\langle d \rangle = 1.00$ and $\sigma(d) = 0.11$ mm; the size distribution is shown in Fig. 4(c) compared to experiments.

In our simulations, we aim to capture the qualitative features of the settling processes. Because the settling dynamics evolve on timescales much larger than a Stokes' settling time, $t_s = a/U_s$, we must simulate over periods of time that are at least $O(10t_s)$. Additionally, we aim to capture the qualitative features of the settling processes, which includes capturing particle-particle interactions and their collective behavior. Thus, our computational domain must include at least $O(10)$ particles, while being sufficiently refined enough to capture the fluid-particle interactions. We use an Eulerian mesh with a nominal mesh size of $\Delta x = a/5$ and a time step of $\Delta t = 1 \times 10^{-3}$ s, corresponding

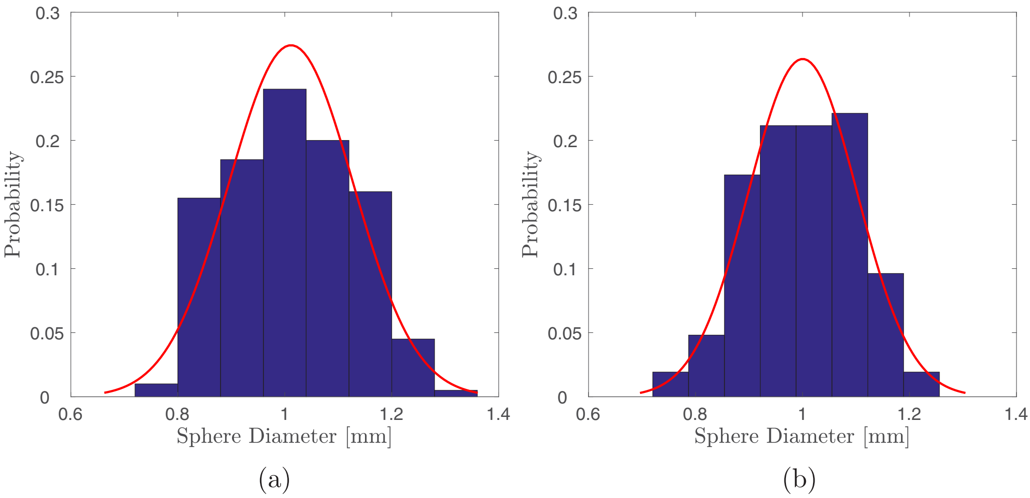

FIG. 4. Probability plots for a sample of sphere diameters used in (a) experiments and (b) simulation. Normal distributions are overlayed (red lines).

to a settling CFL (Courant–Friedrichs–Lewy) number of $U_s \Delta t / \Delta x < 0.002$. In Sec. IV B, we show that this level of mesh and time refinement is sufficient for capturing the settling dynamics of two interacting particles in a viscoelastic fluid.

In all simulations, the number of particles was $N_p = 104$. When calculating the volume fraction of this suspension, we used an effective radius $a_{\text{eff}} = a + \Delta x$, i.e., the sum of the nominal average particle radius $a = \langle d \rangle / 2$ and the nominal Eulerian mesh size $\Delta x$. The Eulerian mesh size sets the length scale for the spreading of the particle's indicator function, which describes what regions of the Eulerian domain contain the rigid particle and therefore move according to rigid body motion. Thus, the particle volume fraction in our simulations with $N_p = 104$ is $\phi = 4\pi a_{\text{eff}}^3 N_p / (3 L_x L_y L_z) = 0.047$. Unless otherwise noted, particle positions are initially random, with the only constraint that no two particles' center of masses are within $3a$ initially or within $2a$ of a wall (i.e., there is a separation of one nominal particle radius between particle surfaces and the channel walls).

To prevent the unphysical overlap of a particle with another particle or with the wall, we employ a repulsive collision model, as has been described and validated previously for this IB method [27,28]. In this repulsive collision model, proposed by Glowinski *et al.* [52], a short-range repulsive force is exerted when colliding surfaces become close (e.g., closer than the Eulerian mesh resolution $\Delta x$).

### B. Numerical validation

A number of validation tests for the immersed boundary (IB) method were presented by Krishnan *et al.* [27]. This IB code has also been used to simulate the rheology of a suspension of rigid particles in Boger fluids, with good agreement with boundary-fitted simulations [28]. In this subsection, we present a validation case that is relevant to our problem: the collective motion of two rigid spherical particles settling initially side-by-side in a viscoelastic fluid.

We consider the dynamics of two spherical particles settling in a cylindrical tube filled with an Oldroyd-B fluid. We compare to the work of Hu *et al.* [53], who used a 3D arbitrary Lagrangian-Eulerian (ALE) scheme, and Pan and Glowinski [25], who used a 3D fictitious domain/distributed Lagrange multiplier (FD/DLM) method to study this problem. The constitutive equation for an Oldroyd-B fluid can be written as in Eqs. (5) and (6), taken in the limit as $L \to \infty$.

In this problem, two spheres with equal radii $a$ settle through a cylindrical tube of radius $R = 5a$. The spheres are initially positioned side-by-side with $\delta = 3a$. The cylinder has a height $L_z$ with periodic boundary conditions on the top and bottom wall with no net flow, as described in

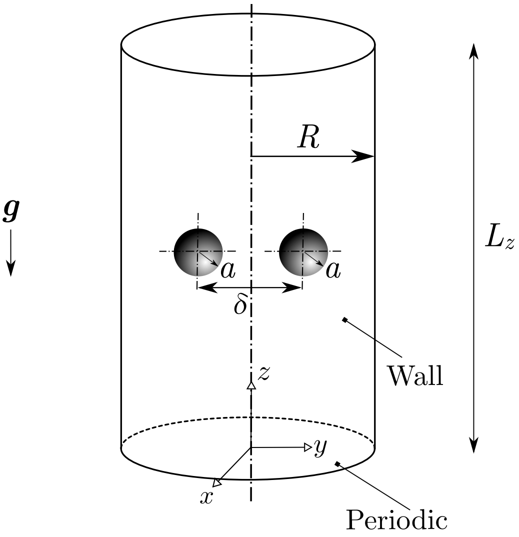

FIG. 5. Schematic used for two spheres, initially side-by-side, settling in a cylindrical tube.

Sec. IV A. The domain was discretized with tetrahedral elements, with mesh symmetry enforced along the $y$ plane. A schematic of the domain is shown in Fig. 5. The fluid is an Oldroyd-B fluid with $\eta_0 = 3.0$ Pa s, $\lambda = 0.1$ s, $\beta = \eta_s/\eta_0 = 0.125$, and $\rho_f = 868\,\text{kg/m}^3$. The sphere has a radius $a = 0.01$ m and density $\rho_s = 2\rho_f = 1736\,\text{kg/m}^3$. A repulsive collision model is again employed, with a collision force prefactor of 0.001 N. No repulsive collision prefactor was reported in Hu *et al.* [53] or Pan and Glowinski [25].

Our results are shown in Fig. 6, compared with the results of Hu *et al.* [53] and Pan and Glowinski [25]. The spheres are attracted and move toward one another, forming a doublet. At this point, the

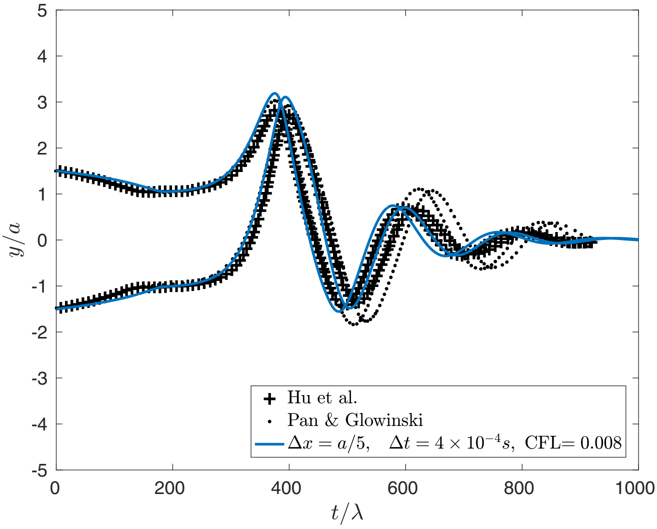

FIG. 6. Trajectory of two spheres, initially side-by-side, settling in an Oldroyd-B fluid with $\beta = \eta_s/\eta_0 = 0.125$. For a single sphere, Re = 0.22 and $\Theta = 0.19$. A comparison is made to the simulation results from Hu *et al.* [53] and Pan and Glowinski [25].

TABLE II. Single sphere settling experiments ($N = 6$).

| Settling velocity [mm/s] | Fluid | |
|---|---|---|
| | Newtonian | Viscoelastic |
| Stokes' prediction, $U_s$ | $0.232 \pm 0.003$ | $0.231 \pm 0.008$ |
| Wall-corrected prediction, $U_{s,w}$ | $0.209 \pm 0.003$ | – – |
| Measured, $U_{z,1}$ | $0.208 \pm 0.005$ | $0.224 \pm 0.010$ |

repulsive collision model is activated and fluid is slowly squeezed out from between the spheres. A doublet falling side-by-side in a viscoelastic fluid is unstable, and the doublet rotates, falling diagonally toward the cylinder wall, before eventually orienting into a vertical "chain" and settling down the centerline of the tube. As mentioned above, this *drafting, kissing, and chaining* behavior of attraction for two spheres settling in a viscoelastic fluid is observed in both simulations and experiments [1]. The agreement between our results and those from the literature is encouraging considering three different methods were used (ALE, FD/DLM, and IB). In our simulation, we use a single Eulerian mesh of size $\Delta x = a/5$ and CFL $= 0.008$. The result from Pan and Glowinski [25] uses similar Eulerian grid resolution ($\Delta x = a/6$).

## V. EXPERIMENTAL RESULTS

Two sets of experiments were performed: first, we study a suspension settling in a quiescent Newtonian fluid and compare it to a suspension settling in a quiescent viscoelastic Boger fluid, discussed in Sec. V A. Second, we study a suspension settling in a cross sheared viscoelastic Boger fluid and compare it to the quiescent results, discussed in Sec. V B. For each set of experiments, two replicate trials were performed to estimate the experimental error. This experimental error captures some of the variability attributable to the initial mixing process, one of the most challenging conditions to control between the experiments.

Before discussing the suspension experiments, we briefly present the results for a single particle settling at the midplane of the static settling cell. As discussed in Sec. II, the characteristic scales we choose for this problem are the particle radius ($a$) as the characteristic length, the terminal speed of a single particle settling at the channel midplane ($U_{z,1}$) as the characteristic velocity, and the time it takes to settle one particle radius ($t_1 = a/U_{z,1}$) as the characteristic time. Thus, these single particle experiments provide the characteristic velocity and timescales that we will use to nondimensionalize the results from the suspension experiments.

In the presence of confining walls, a drag correction factor $K_N$ can be applied to Stokes' settling law in Eq. (1). For weakly confined particles such as in this experiment, where $\epsilon = d/W = 0.1$, Faxén's correction [54] can be used and $K_N(\epsilon = 0.1) = 1.11$. The wall-corrected Stokes' settling speed then becomes

$$U_{s,w} = \frac{2}{9}\frac{(\rho_s - \rho_f)a^2 g}{\eta K_N}. \tag{10}$$

A small sample of painted spheres were used to measure the settling rate of single particles in both fluids. The results are shown in Table II. The error shown for the Stokes' settling velocity and the wall-corrected Stokes' settling velocity is from the propagation of error from the measured particle radii in the sample. For this small sample, spheres with particle radii near the mean measured value given in Sec. III D were selected to minimize sampling error. The particle settling rates were measured both manually (i.e., measuring the time for a sphere to settle a given displacement) and using the particle tracking method described in Sec. III D; the results differed by less than 1% and any differences were within the experimental error recorded in Table II. The measured settling rate in the Newtonian fluid quantitatively matched that predicted from a wall-corrected Stokes' velocity.

For the viscoelastic fluid, the Stokes' settling velocity was estimated from Eq. (1) using the fluid's zero-shear viscosity $\eta_0$. No wall-corrected estimate was made for the viscoelastic fluid because the drag correction due to the presence of confining walls is not generally known for viscoelastic fluids. The measured settling rate was slightly higher than in the Newtonian fluid. From the measured settling velocity, we can calculate the sedimentation Weissenberg number for a single particle as $\Theta_1 = \lambda U_{z,1}/(2a) = 0.25$. As reviewed by Chhabra [55] and McKinley [56], a small drag reduction on particles settling in viscoelastic Boger fluids at $\Theta < 1$ is typical.

### A. Suspensions settling in a quiescent fluid

In this first set of experiments, we study the settling behavior of rigid, non-Brownian spherical particles in a quiescent Newtonian fluid and a viscoelastic Boger fluid. Images from the initial stages of a typical static sedimentation experiments in both the Newtonian and viscoelastic Boger fluids are compared side-by-side in Fig. 7. The images show the tracked particles (in white) with multiple frames superimposed to show the trajectories and relative velocities of the particles as they settle. Each snapshot shows the trajectories of particles over a time period of $\Delta t^* \approx 2$ beginning from the labeled time, where $t^* = t/t_1 = tU_{z,1}/a$. Recall that only 10% of the particles are tracked. In both fluids, larger scale velocity fluctuations are observed initially and decay over time. These velocity fluctuations are significantly more pronounced in the viscoelastic Boger fluid. Initially, large clusters of particles are observed settling quickly in the viscoelastic fluid. As these large clusters leave the viewing window, smaller scale vertically oriented "streamers" of particles, alternating with regions of relatively clarified fluid, are observed. These streamers eventually settle out of the viewing window, leaving behind relatively clarified fluid. It is clear from these snapshots that the initial transient settling process is faster and more inhomogeneous in the viscoelastic Boger fluid compared to the Newtonian fluid. A movie showing this settling process in the Newtonian and viscoelastic Boger fluids side-by-side is included in the Supplemental Material [57]. The remainder of this section attempts to describe the settling processes in the two fluids quantitatively to highlight these differences.

Histograms of the particle velocities from a typical static sedimentation experiment in both the Newtonian and viscoelastic Boger fluids are shown in Fig. 8. In each figure, we plot the probability density function (PDF) for the lateral velocity $U_x$ and the settling velocity $U_z$, both normalized by the terminal speed of a single sphere settling at the cell midplane in that same corresponding fluid, $U_{z,1}$ (from Table II). The histograms show the measured velocities of all tracked particles over the course of the entire experiment. The mean $\langle\cdot\rangle$ and standard deviation $\sigma(\cdot)$ of the lateral and settling velocities are shown in Table III. The mean and standard deviation were calculated from the measured velocities of all tracked particles over the course of the entire experiment, and were averaged over two trials.

In the Newtonian fluid, the normalized mean settling velocity is less than one, signifying a hindered settling velocity relative to a single sphere settling at the cell midplane. The lateral velocity distribution is centered around zero, and both velocity distributions exhibit significant fluctuations about the mean. The standard deviation of the settling velocities is approximately a factor of two larger than for the lateral velocities, in reasonable agreement with that observed previously for steady settling processes in Newtonian fluids, as reviewed by Guazzelli and Hinch [4]. In the viscoelastic Boger fluid, the normalized mean settling velocity is greater than one, signifying an enhanced settling velocity relative to a single sphere. The velocity fluctuations in the lateral and settling directions are also enhanced in the viscoelastic fluid relative to the Newtonian fluid. In the settling direction, the velocity fluctuations are approximately the same magnitude as the mean particle velocity.

The PDFs and mean and standard deviation of the velocities highlight important differences between the settling behavior in the two fluids. However, they also mask the time dependent

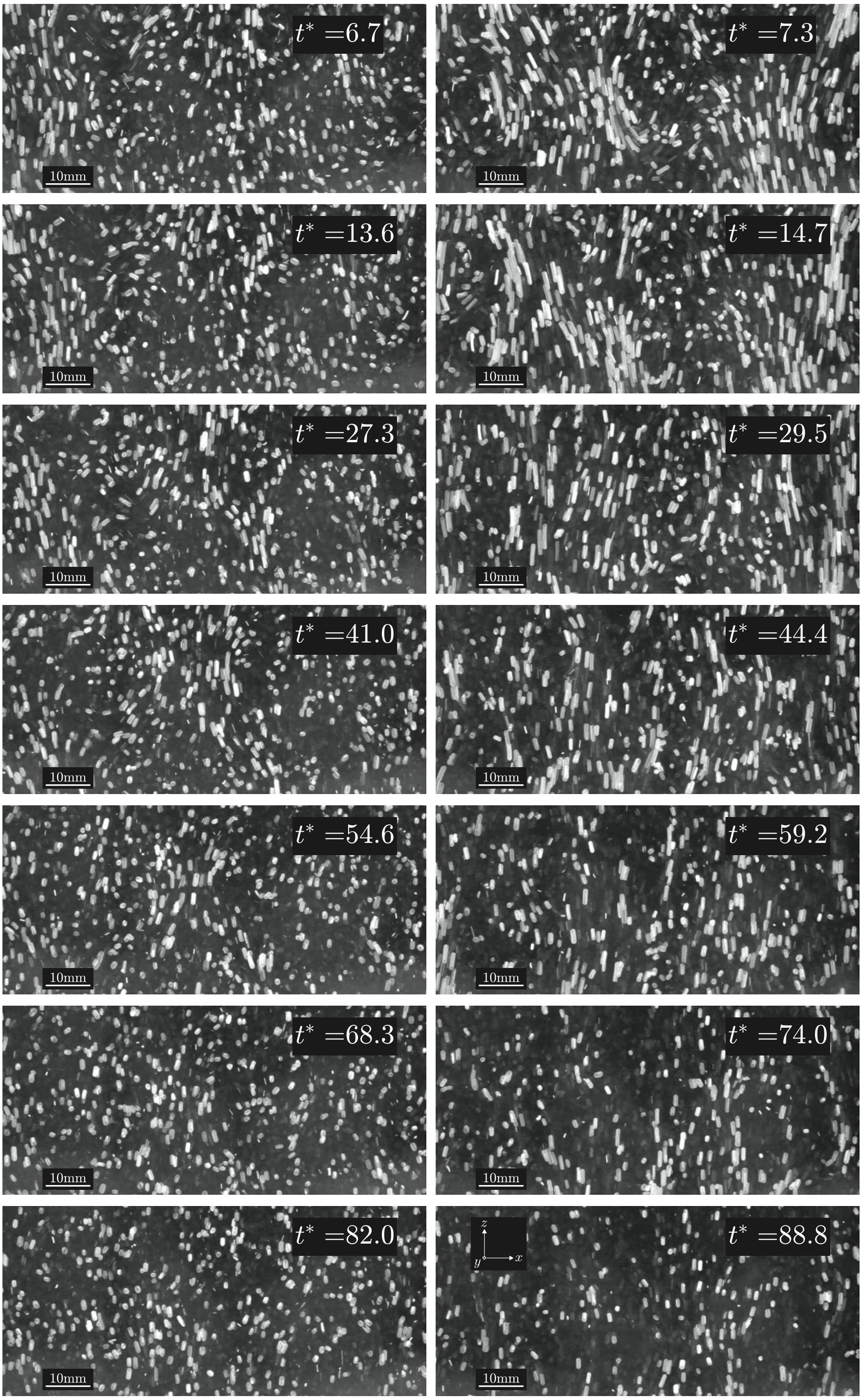

(a) (b)

FIG. 7. Superimposed images showing trajectories of the settling spherical particles in the (a) Newtonian and (b) viscoelastic fluid during a static sedimentation experiment.

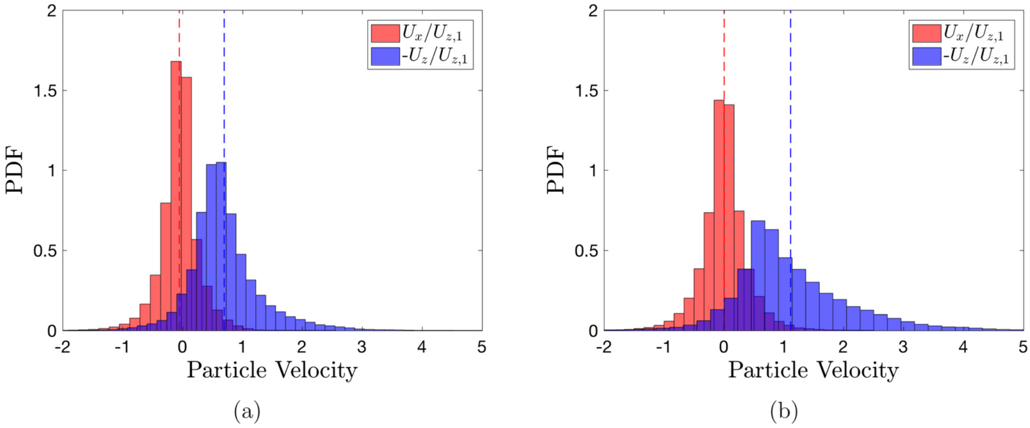

FIG. 8. Probability density functions for the particle settling velocity (blue) and lateral velocity (red) during the course of a typical static sedimentation experiment in the (a) Newtonian and (b) viscoelastic fluid. Dashed vertical lines represent the mean.

nature of the settling processes observed in Fig. 7. In Fig. 9, we show the measured (black) and ensemble averaged (yellow) particle settling velocity at each recorded time of the experiment. In the Newtonian fluid, the normalized mean settling velocity decays monotonically from a value of approximately one and the velocity fluctuations decay over time. This is in qualitative agreement with what has been observed in less confined Newtonian suspensions by Guazzelli [58]. From these results, there does not appear to be a significant time period where a steady settling behavior is observed before the suspension interface leaves the viewing window in our experiments. In the viscoelastic Boger fluid, the normalized mean settling velocity and corresponding velocity fluctuations increase at short times to a maximum value of nearly two at $t^* \approx 25$ before decaying as the particle clusters and streamers settle out of the viewing window. A maximum in the mean settling velocity and velocity fluctuations was observed for particles settling in elastic fluids in point-particle simulations by Vishnampet and Saintillan [12], and has also been observed in other unstable settling processes such as for spheroids and deformable particles [17]. As in those prior studies, we propose that the maximum in the mean particle settling rate is a result of a structurally inhomogeneous sedimentation process—involving the formation of fast-settling particle-rich clusters—in a finite-sized settling box with a no-flux bottom boundary. As the particles begin to aggregate, the fast-settling clusters contribute to a rise in the average settling velocity. As these clusters leave the Eulerian viewing window (as in our experiments), and ultimately reach the bottom of the settling box (as in the point-particle simulations of Vishnampet and Saintillan [12] and Saintillan *et al.* [17]), they leave behind more isolated particles and particles settling near a side wall, which settle more slowly, contributing to a subsequent fall in the average settling velocity.

TABLE III. Quiescent settling experiments, $\phi = 0.05$ ($N = 2$).

| | Fluid | |
|---|---|---|
| | Newtonian | Viscoelastic |
| $-\langle U_z\rangle/U_{z,1}$ | 0.72 ± 0.05 | 1.14 ± 0.05 |
| $\sigma(U_z)/U_{z,1}$ | 0.54 ± 0.07 | 1.07 ± 0.21 |
| $\langle U_x\rangle/U_{z,1}$ | −0.03 ± 0.05 | −0.01 ± 0.04 |
| $\sigma(U_x)/U_{z,1}$ | 0.29 ± 0.05 | 0.43 ± 0.10 |

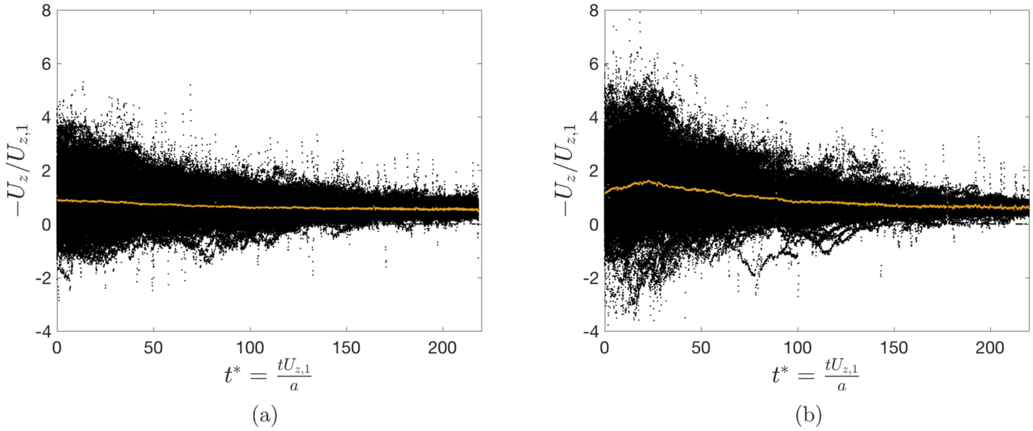

FIG. 9. Individual particle velocities (black dots) and the average of the particle velocity for all tracked particles at $t^*$ (yellow dots) recorded over the course of a typical sedimentation experiment in the (a) Newtonian and (b) viscoelastic fluid.

### B. Suspensions settling in a cross sheared viscoelastic fluid

In this second set of experiments, we study the settling of a suspension of particles in a cross sheared viscoelastic Boger fluid. Before discussing the suspension experiments, we again briefly present the results for a single particle settling at the midplane of the Taylor-Couette flow cell. It is well established that a single sphere settling in a cross sheared Boger fluid experiences a reduction in its settling velocity [33,41,59–61], and so we require a baseline measurement for a single sphere. For a sample of $N = 5$ spheres, at a cross shear Weissenberg number of $\mathrm{Wi} = \lambda\dot{\gamma} = 1.1$, the settling speed for a single sphere was measured to be $U_{z,1}(\mathrm{Wi} = 1.1) = 0.188 \pm 0.011$ mm/s. Comparing to Table II, we observe that the cross shear flow of $\mathrm{Wi} = 1.1$ reduces the single particle settling speed by a factor of approximately 1.2 where $-U_{z,1}(\mathrm{Wi} = 1.1)/U_{z,1} = 0.84 \pm 0.06$. This magnitude of reduction of the particle mobility is comparable with that which has been previously observed experimentally [41,59].

To investigate the effect of a cross shear flow, we perform two experiments in the Taylor-Couette flow cell: a suspension settling under no shear, and a suspension settling with a cross shear Weissenberg number of $\mathrm{Wi} = \lambda\dot{\gamma} = 1.1$. The results are presented in Table IV. For the suspension settling under no shear ($\mathrm{Wi} = 0$), the results match reasonably well to those presented in Table III of Sec. V A, showing that the mixing procedure and image analysis are consistent between the two settling cells. When a cross shear flow is applied at $\mathrm{Wi} = 1.1$, the mean settling rate is drastically reduced, by a factor of nearly 1.9 relative to the case of no cross shear. For the values shown in Table IV, $U_{z,1}$ is the terminal speed for a single particle settling in the viscoelastic fluid at $\mathrm{Wi} = 0$ (shown in Table II). Thus, we see that the mean settling rate is significantly reduced relative to $U_{z,1}$ but also relative to $U_{z,1}(\mathrm{Wi} = 1)$. It is clear from this result that both the cross shear and the finite volume fraction of the suspension act to hinder the mean particle settling velocity.

TABLE IV. Experiments in the Taylor-Couette flow cell with a viscoelastic suspending fluid, $\phi = 0.05$ ($N = 2$).

| | $\mathrm{Wi} = 0$ | $\mathrm{Wi} = 1.1$ |
|---|---|---|
| $-\langle U_z\rangle/U_{z,1}$ | $1.11 \pm 0.29$ | $0.59 \pm 0.07$ |
| $\sigma(U_z)/U_{z,1}$ | $0.93 \pm 0.31$ | $1.29 \pm 0.06$ |

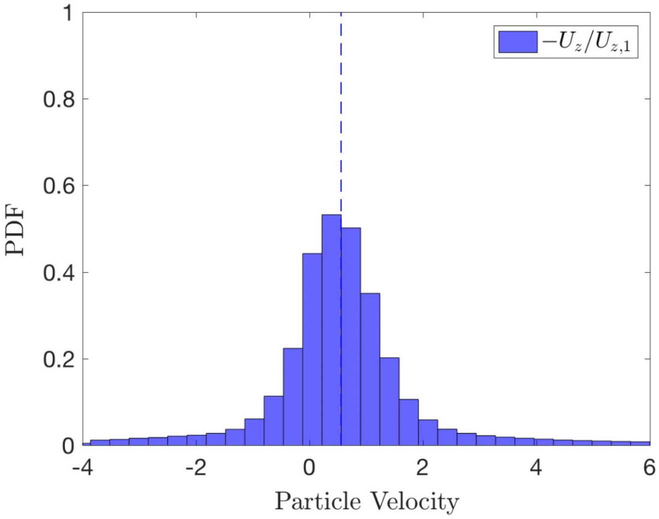

FIG. 10. Probability density function for the particle settling velocity during the course of a typical cross sheared sedimentation experiment in the viscoelastic fluid (Wi = 1.1). The dashed vertical line represents the mean.

A histogram of the particle settling velocities from a typical cross sheared sedimentation experiment in the viscoelastic fluid is shown in Fig. 10. The lateral velocities are not displayed as they are dominated by the shear flow. In this cross sheared case, we observe a nearly symmetric distribution about the mean settling velocity, in contrast to the skewed distribution observed in the quiescent settling case.

## VI. SIMULATION RESULTS

A computational study was performed, using the numerical tool described in Sec. IV, to further investigate the settling phenomena observed experimentally. As before, two sets of simulations were performed: first, we study a suspension settling in quiescent Newtonian and viscoelastic Boger fluids, discussed in Sec. VI A. Second, we simulate a suspension settling in cross sheared viscoelastic Boger fluids, discussed in Sec. VI B. Whenever possible, we compare directly to our experimental results.

The goal of this computational study was to recreate the physics observed experimentally and to use our simulation tool to examine physical mechanisms within the settling suspensions. There are several benefits to studying this problem computationally. For example, we are afforded control of the initial condition beyond that which can be achieved experimentally: we can begin with the exact same particle configuration when comparing the settling behavior between different fluids or different flow conditions. Additionally, we can more easily sweep across parameters to explore the effect of viscoelasticity. In the following subsections, we will consider three suspending fluids: (1) a Newtonian fluid with the same properties shown in Table I; (2) a viscoelastic Boger fluid as shown in Table I; and (3) a strongly viscoelastic Boger-like fluid with the properties shown in Table I except with a polymer relaxation time that is 4 times longer, i.e., $\lambda = 4.4$ s. The elastic stress ratio coefficient, $\psi_{1,0}/\eta_0 = 2(1-\beta)\lambda = 6.2$ s, is therefore also 4 times larger in the strongly viscoelastic Boger-like fluid.

Before discussing the suspension simulations, we briefly present the results for a single particle settling at the midplane of the computational domain. The results are shown in Table V. Comparing to Table II, we observe reasonable agreement in the magnitude of the settling speed for a single particle settling in the Newtonian and viscoelastic Boger fluid. There is a slight drag reduction

TABLE V. Single sphere settling simulations.

| Settling velocity [mm/s] | Newtonian | Viscoelastic $\Theta_1 = 0.27$ | Viscoelastic $\Theta_1 = 1.0$ |
|---|---|---|---|
| Calculated, $U_{z,1}$ | 0.221 | 0.246 | 0.227 |

for the particle with $\Theta_1 = \lambda U_{z,1}/(2a) = 0.27$, as observed experimentally. For the particle in the strongly viscoelastic fluid with $\Theta_1 = 1.0$, the drag increases again, as is typical for most Boger-like fluids as $\Theta$ becomes $O(1)$ [55,56].

### A. Suspensions settling in a quiescent fluid

Using numerical simulations, we first examine the settling behavior of rigid spherical particles in a quiescent Newtonian fluid, a viscoelastic Boger fluid, and a strongly viscoelastic Boger-like fluid. The initial condition is identical between the three cases. In these simulations, we begin from a slightly perturbed particle concentration distribution, with more particles located on the left side (negative $x$ half-space) of the computational box. This was done to mimic the initial condition from the experiments, which was following random mixing. It has been suggested that random mixing—i.e., if the particles are placed randomly and independently—results in statistical fluctuations in the particle number of $O(\sqrt{N_p})$ [4,62,63]. Thus, we begin with approximately $N_p/2 + \sqrt{N_p}$ particles on the left side ($x < 0$) of the computational box and $N_p/2 - \sqrt{N_p}$ on the right side to intentionally seed a concentration perturbation. In our simulations, we had a total of $N_p = 104$ and overall volume fraction of $\phi = 0.047$, with $N_p(x < 0, t^* = 0) = 61$ and $\phi(x < 0, t^* = 0) = 0.055$, and $N_p(x \geqslant 0, t^* = 0) = 43$ and $\phi(x \geqslant 0, t^* = 0) = 0.039$. We propose that this magnitude of concentration fluctuation—or possibly greater [64]—was likely present in our experiments. Here, we set it intentionally, with the goal of observing whether the perturbation grows or decays in the different test fluids.

Snapshot images from the quiescent sedimentation simulations in the three fluids are compared in Fig. 11. The images show interpolated values of the velocity on the surface of all particles as well as on a slice through the midplane ($y = 0$) of the computational domain, such that we are viewing the negative $y$ half-space of the domain. All particles in the negative $y$ half-space of the domain are visualized. At early times, we observe similar behavior between the three fluids, since all started with the same initial particle configuration. As time progresses, the velocity fluctuations do not appear to grow from their initial value in the Newtonian fluid and the suspension remains homogeneous at long times. In the viscoelastic fluids, the velocity fluctuations appear to grow in time, eventually forming a particle-rich “streamer” of fast settling particles and a backflow region that is relatively devoid of particles after $t^* \approx 50$. This streamer formation appears to form more quickly in the strongly viscoelastic fluid, appearing for $t^* < 50$. These results qualitatively match what was observed experimentally, with a more inhomogeneous settling process observed in the viscoelastic fluids.

Histograms of the particle velocities from the static sedimentation simulations in both the Newtonian and viscoelastic Boger fluids are shown in Fig. 12. The PDFs for the lateral velocity $U_x$ and settling velocity $U_z$ are both normalized by the terminal speed of a single sphere settling at the midplane of the computational domain (from Table V). The histograms contain the measured velocities of all particles recorded following an initial period of $\Delta t^* = 20$, i.e., the time it would take for a single particle at the midplane to settle approximately one computational box height. The simulations were run for a minimum time of $t^* > 88$ ($t = 200$ s), such that a single particle would settle through the computational box 4–5 times. The PDFs show reasonable qualitative agreement to those observed experimentally and shown in Fig. 8. In both the experiments and simulations, the mean settling rate in the viscoelastic fluids is higher than in the Newtonian fluid, driven by

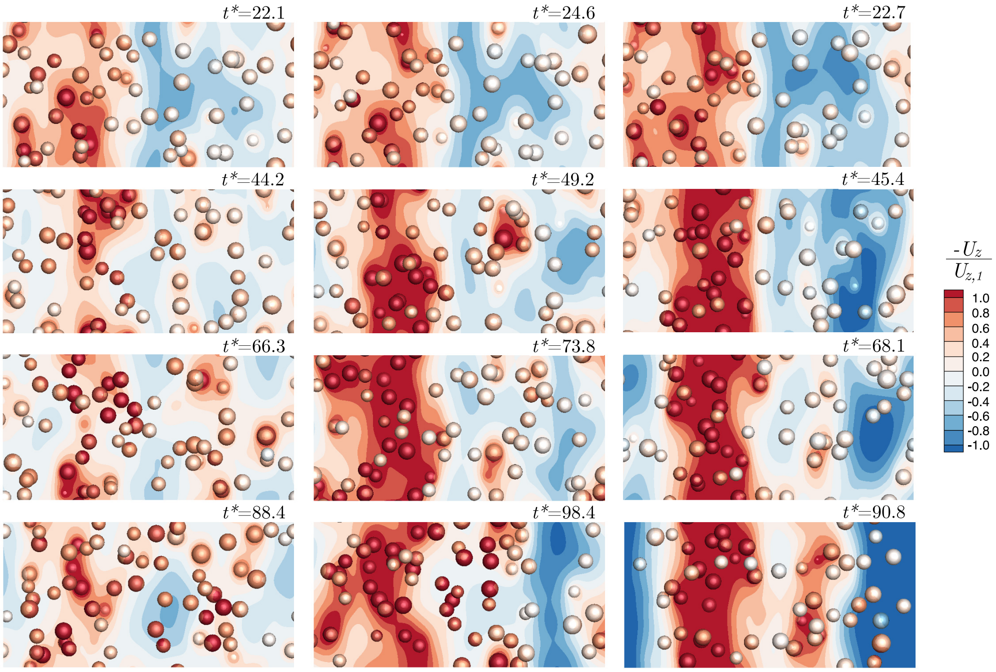

(a) (b) (c)

FIG. 11. Velocities of the settling particles over time in the (a) Newtonian, (b) viscoelastic ($\Theta_1 = 0.27$), and (c) strongly viscoelastic ($\Theta_1 = 1.0$) fluids. Interpolated values of the velocity are shown on the surface of the particles as well as on a slice through the midplane of the computational domain. Velocities in red are aligned with gravity and velocities in blue indicate backflow.

an extended tail of higher settling velocities which becomes more pronounced in the strongly viscoelastic fluid.

The mean $\langle\cdot\rangle$ and standard deviation $\sigma(\cdot)$ of the lateral and settling velocities are shown in Table VI. In the Newtonian fluid, we observe good agreement between the normalized mean settling velocity in the simulation compared to the experiments. The simulations show a larger standard deviation for the settling velocities compared to the lateral velocities, as in the experiments, although the velocity fluctuations are underpredicted by a factor of approximately two compared to

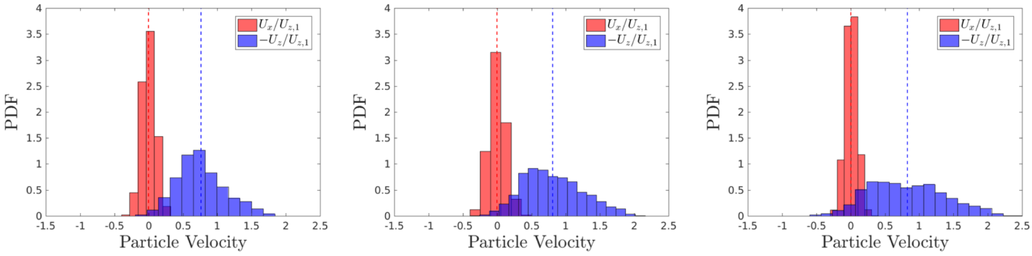

(a) (b) (c)

FIG. 12. Probability density functions for the particle settling velocity (blue) and lateral velocity (red) during the course of the initially perturbed static sedimentation simulation in the (a) Newtonian, (b) viscoelastic fluid ($\Theta_1 = 0.27$), and (c) strongly viscoelastic fluid ($\Theta_1 = 1.0$). Dashed vertical lines represent the mean.

TABLE VI. Quiescent simulations, $\phi = 0.05$.

| | Newtonian | Viscoelastic $\Theta_1 = 0.27$ | Viscoelastic $\Theta_1 = 1.0$ |
|---|---|---|---|
| $-\langle U_z\rangle/U_{z,1}$ | 0.76 | 0.81 | 0.83 |
| $\sigma(U_z)/U_{z,1}$ | 0.31 | 0.43 | 0.55 |
| $\langle U_x\rangle/U_{z,1}$ | −0.01 | 0.00 | 0.00 |
| $\sigma(U_x)/U_{z,1}$ | 0.11 | 0.12 | 0.09 |

the experiments. In the viscoelastic fluids, the mean settling velocity is slightly higher than in the Newtonian fluid, but still hindered relative to a single spherical particle settling at the midplane.

Thus far, we have observed a few key differences between the simulations and the experiments: namely, an underprediction of the velocity fluctuations and an underprediction of the mean settling rate in the viscoelastic fluid. The velocity fluctuations in both the lateral and settling directions are larger in the experiments, illustrated in the PDFs and also captured in the standard deviation. We propose that this could be primarily attributable to the small computational domain used in the simulations. Clearly, the lateral dimension is important, as it dictates the largest length scale over which concentration fluctuations can occur at a given vertical position in the suspension. In the experiments, the settling cell had a lateral dimension of $L_x \approx 500a$, whereas in the simulations, the computational domain had $L_x = 40a$. Indeed, as seen in Fig. 7, the initially large lateral velocity fluctuations occur on length scales larger than the computational box. This may also help to explain the underprediction in the mean settling velocity in the viscoelastic fluid.

Additionally, although the single-mode FENE-P model utilized in this study captures the key rheological behavior of the polymeric fluid used in the experiments, certain aspects are not well captured, as seen in Fig. 1 and discussed in Sec. IV. The lateral drift of single particles settling in a viscoelastic shear flow has been attributed to the imbalance of polymer stretching on either side of the particle, resulting in an imbalance of normal stresses [15,65]. By fitting to a single (longest) relaxation mode, the short-time normal stress response is underpredicted in the FENE-P model, as observed in Fig. 1(b). As discussed in Sec. I, a shear thinning viscosity can contribute to particle cluster formation; we see in Fig. 1(a) that the shear thinning viscosity is more abrupt in the model than in the experimental fluid. Both discrepancies could contribute to the differences observed between our experiments and numerical simulations.

In Fig. 13, the time evolution of the ensemble averaged particle settling velocity and standard deviation is plotted. In the Newtonian fluid, the mean settling velocity remains roughly constant throughout the simulation, increasing slightly to a maximum value of 0.79 at long times. The

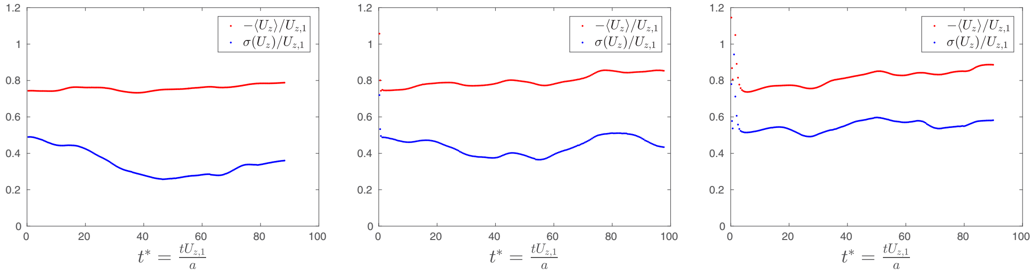

(a) (b) (c)

FIG. 13. Ensemble averaged particle velocities (red dots) and standard deviation (blue dots) for tracked particles at a given $t^*$ over the course of a sedimentation simulation in the (a) Newtonian, (b) viscoelastic fluid ($\Theta_1 = 0.27$), and (c) strongly viscoelastic fluid ($\Theta_1 = 1.0$).

TABLE VII. Single sphere cross shear simulations.

| | $\Theta_1 = 0.27$ | | $\Theta_1 = 1.0$ | |
|---|---|---|---|---|
| | Wi = 1 | Wi = 4 | Wi = 1 | Wi = 4 |
| $-U_{z,1}(\mathrm{Wi})/U_{z,1}$ | 0.77 | 0.38 | 0.78 | 0.40 |

velocity fluctuations in the Newtonian fluid decay slightly at short times, matching what was observed qualitatively in Fig. 11, and do not exceed their initial value during the course of the simulation. In the viscoelastic Boger fluid, the mean settling velocity grows throughout the simulation, reaching a maximum value of 0.85. The velocity fluctuations initially decay slightly, as in the Newtonian fluid, but then grow and return to their initial value at longer times, and at times exceed the initial value. In the strongly viscoelastic fluid, both the mean settling rate and the velocity fluctuations grow throughout the simulation, with the mean settling rate reaching a maximum value of 0.89 at the final recorded time point.

It is interesting to note that, in our simulations, we did not observe a maximum in the mean settling velocity followed by a decay at longer times, as was observed in our experiments (cf. Fig. 9). As discussed in Sec. V A, this maximum was proposed to be a result of the aggregation and clustering of particles, which caused them to settle more quickly, rapidly leaving the viewing window and approaching the bottom of the settling box, thus leaving behind particle-depleted regions with slower moving particles. Therefore, we believe the absence of the maximum in the simulations to be primarily the result of the periodic boundary condition for particles in the settling direction. In our simulations, although there is no net flux through the system, fast-settling clusters of particles re-enter the periodic computational box. Eventually, we believe the mean particle settling rate in our simulations would plateau and fluctuate around a long-time value, rather than exhibiting a maximum and decaying, resulting from a balance between particle aggregation and hydrodynamic dispersion.

### B. Suspensions settling in a cross sheared viscoelastic fluid

In this second set of simulations, we return to the settling of particles in cross sheared viscoelastic fluids. The reduction in the settling velocity of a single particle is summarized in Table VII. We observe a reduction in the settling velocity as a function of the cross shear Weissenberg number $\mathrm{Wi} = \lambda\dot{\gamma}$, for both the viscoelastic Boger fluid ($\Theta_1 = 0.27$) and the strongly viscoelastic Boger-like fluid ($\Theta_1 = 1.0$). At Wi = 1, the settling velocity reduction is similar in magnitude (and slightly overpredicted) compared to that observed experimentally, where $-U_{z,1}(\mathrm{Wi} = 1.1)/U_{z,1} = 0.84 \pm 0.06$, as presented in Sec. V B.

To test the effect of a cross shear flow on a suspension of particles, we used the same computational box as before, with the walls in the y-direction moving with velocity $u_i = (\pm\dot{\gamma}W/2, 0, 0)$ at $y = \pm W/2$. It should be noted that a rectangular computational box is used, and the curvature of the velocity profile (present in the experimental Taylor-Couette flow cell) was neglected. In these simulations, we allow the suspensions to settle for at least $t^* > 45$ ($t = 100$ s).

For a suspension of particles at a volume fraction of $\phi = 0.05$, we find that the mean settling velocity is reduced below that for a single particle (shown in Table V). The results for a suspension of particles are summarized in Table VIII. The mean settling velocity is reduced as a function of the cross shear Weissenberg number $\mathrm{Wi} = \lambda\dot{\gamma}$ for both simulated fluids. Again, the settling velocity reduction is similar in magnitude to what was observed experimentally, where at Wi = 1.1, $-\langle U_z\rangle/U_{z,1} = 0.59 \pm 0.07$, as presented in Sec. V B. In agreement with the experiments, our simulations suggest that both the cross shear and the finite volume fraction of the suspension act to hinder the mean particle settling velocity in viscoelastic suspending fluids.

TABLE VIII. Cross shear simulations, $\phi = 0.05$.

| | $\Theta_1 = 0.27$ | | $\Theta_1 = 1.0$ | |
|---|---|---|---|---|
| | Wi = 1 | Wi = 4 | Wi = 1 | Wi = 4 |
| $-\langle U_z\rangle/U_{z,1}$ | 0.63 | 0.31 | 0.64 | 0.33 |
| $\sigma(U_z)/U_{z,1}$ | 0.38 | 0.38 | 0.34 | 0.24 |

In Fig. 14, we show a histogram of the particle settling velocities recorded during a simulation for $\Theta_1 = 0.27$ and Wi = 1 in the viscoelastic Boger fluid. We observe a more symmetric distribution of particle velocities than that observed in the quiescent settling case shown in Fig. 12(c). Comparing with Fig. 10, this qualitatively matches what was observed experimentally. In the following section, we discuss possible explanations for this behavior.

## VII. DISCUSSION

In the previous two sections, we presented a number of results from both experiments and numerical simulations on the behavior of settling suspensions and the effects of fluid elasticity and a cross shear flow. We begin by summarizing these results in Sec. VII A. We then discuss possible physical mechanisms for the observed behavior in Sec. VII B.

### A. Summary of findings

The first aim of this work was to identify the salient differences between the quiescent settling behavior of a suspension of spherical particle in a Newtonian and a viscoelastic Boger fluid. In Sec. V A, we presented experimental results showing a characteristically distinct settling process in the two suspending fluids. In the Newtonian fluid, the settling rate was hindered relative to the settling speed of a single particle, with velocity fluctuations that decreased following mixing. This behavior is in qualitative agreement with what has been observed in less confined suspensions in

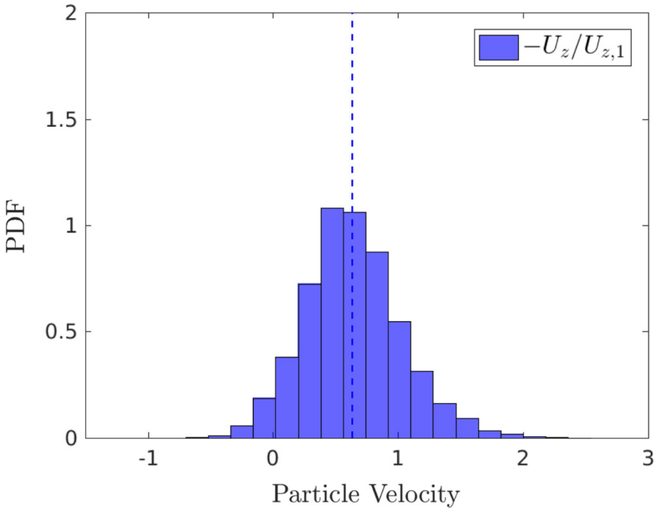

FIG. 14. Probability density function for the particle settling velocity during the course of a cross sheared sedimentation simulation in the viscoelastic fluid ($\Theta_1 = 0.27$, Wi = 1). The dashed vertical line represents the mean.

Newtonian fluids [4]. In the viscoelastic Boger fluid, the settling process was time-dependent and inhomogeneous: following mixing, large clusters of particles settled quickly out of the suspension, transitioning into smaller scale vertically aligned streamers. This resulted in a ensemble-averaged settling rate and corresponding velocity fluctuations that grew to a maximum value at short times ($t^* < 50$) before decaying. This initially fast settling resulted in an overall mean settling rate (ensemble and time-averaged) that was faster than that for a single particle. This enhanced and inhomogeneous settling behavior in a viscoelastic fluid is in qualitative agreement with what has been observed before in other viscoelastic [6,7] or shear-thinning and weakly viscoelastic fluids [8,9].

The experimental results were qualitatively supported by the numerical simulations presented in Sec. VI A. In the simulations, a small perturbation in the particle concentration was set initially to mimic a suspension following random mixing. A Newtonian fluid and two viscoelastic fluids were tested: a Boger fluid with parameters fit to our experimental rheology data and a strongly viscoelastic fluid with a longer fluid relaxation time. In the viscoelastic fluids, both the mean settling rate and velocity fluctuations were enhanced relative to that in the Newtonian fluid, and this effect increased as a function of the fluid relaxation time. In the viscoelastic fluids, the initially perturbed state led to the formation of a vertical stream of fast settling particles and a region of relatively clarified, backflowing fluid. The formation of a vertical stream appeared to develop more quickly in the strongly viscoelastic fluid. However, in both the Newtonian and viscoelastic fluids, the overall mean settling rate was still hindered relative to the settling speed of a single particle. This was attributed primarily to the small computational box, which cut off the length scale for the largest possible velocity fluctuation. Both the experiments and numerical simulations suggest that a collective behavior occurs during the sedimentation of a suspension of particles in a viscoelastic fluid which results in the aggregation of particles as they settle. A possible explanation for this behavior is proposed in the following section, Sec. VII B.

The second aim of this work was to evaluate the effect of a cross shear flow on the settling behavior of a suspension of particles in a viscoelastic Boger fluid. When a cross shear flow was applied in the Boger fluid ($\mathrm{Wi} \approx 1$), the particle mean settling rate was drastically reduced, below that predicted for a single particle. This result was supported by both experiments and numerical simulations. This reduction in the mean settling rate was observed in simulations for both fluids across the range of tested sedimentation and shear Weissenberg numbers. In the following section, we discuss possible explanations for this behavior.

### B. Physical mechanisms

In a Newtonian fluid, it is well known that a suspension of particles settles with a hindered mean settling velocity relative to the Stokes' law prediction for a single particle. Batchelor [5] showed that in a homogeneous and randomly mixed suspension, this hindered settling was primarily due to fluid backflow. As particles settle, they entrain fluid with them, pulling the fluid toward the bottom of the container. Due to the bottom wall of the container, there is no mean flux through a given horizontal cross-section of the box, and some fluid must be forced up through the suspension. For a volume fraction of $\phi = 0.05$, the widely used Richardson-Zaki empirical correlation predicts $\langle U\rangle/U_s \approx 0.77$; our experimental and simulation results are in reasonable agreement with this prediction. Due to the diffusive motion of the particles [66], a randomly mixed suspension remains structurally homogeneous. Several hypotheses regarding why velocity fluctuations decay from their initial value following mixing have been proposed, as reviewed by Guazzelli and Hinch [4].

In a viscoelastic fluid, the aggregation of clusters of particles has been observed in both shear-thinning fluids with small normal stress differences [8,9] and in viscoelastic fluids [6,7]. As outlined in Sec. I, two theories have been proposed to explain how local aggregation of particles can result in a structural concentration instability during sedimentation [11,12]. Both theories consider this structural concentration instability to depend on a competition between a lateral drift of particles toward one another in a viscoelastic fluid and a hydrodynamic dispersion that acts to maintain suspension homogeneity. In the work of Phillips [11], the effective flux of particles toward one another was assumed to fundamentally arise from direct particle-particle interactions, e.g., as calculated for a pair of identical particles in a second-order fluid [20]. For a suspension of settling particles with a concentration profile initially perturbed in the horizontal direction, this flux competes with hydrodynamic dispersion, and under certain conditions, can result in the growth of particle-rich columns. Vishnampet and Saintillan [12] performed a similar linear stability analysis using the second-order fluid model to describe the same effect, but considered a different driving force for the flux of particles toward particle-rich regions. They suggested that a weak concentration fluctuation (e.g., due to random mixing) creates a local velocity disturbance which points down in particle-rich regions and up in a particle-depleted regions. For a particle settling in the flow direction of linear shear flow in a viscoelastic fluid, a lateral migration is predicted to arise at $O(\mathrm{Wi})$ [12–14]. This lateral migration pushes particles toward streamlines aligned with the settling motion, i.e., toward regions of higher density and particle concentration. These regions settle faster, reinforcing any initial concentration perturbation. From the standpoint of a linear stability analysis, this can give rise to a concentration instability.

Phillips' theory [11] predicted the timescale at which concentration fluctuations would grow, above a critical length scale, as

$$t_P^* = \frac{4\pi^2}{27}\left(\frac{1}{(1-\beta)\Theta_1\phi}\right). \tag{11}$$

Vishnampet and Saintillan's theory showed that the longest wavelength fluctuations grow the fastest and smaller wavelength fluctuations are damped by hydrodynamic diffusion. For the zero-wave-number mode, the timescale for concentration fluctuation growth (i.e., the inverse growth rate) was

$$t_{\mathrm{VS}}^* = \frac{1}{9}\left(\frac{1}{k_l(1-\beta)\Theta_1\phi}\right), \tag{12}$$

where $k_l$ is a lateral lift force coefficient for a spherical particle settling in the flow direction of a local shear flow. Interestingly, both theories predict the same scaling for the growth rate of concentration fluctuations as $[(1-\beta)\Theta_1\phi]^{-1}$. In Sec. VI A, we qualitatively observed a faster growth rate of velocity fluctuations as $\Theta_1$ was increased. To compare these predictions with our experiments with the viscoelastic Boger suspending fluid, we use $\beta = 0.30$, $\Theta_1 = 0.25$, and $\phi = 0.05$. As for the value of $k_l$, we use the value $k_l = 1/2$, as calculated by Einarsson and Mehlig [14] and compared to by Zhang *et al.* [15], rather than the value suggested by Vishnampet and Saintillan [12]. Using our experimental values we find $t_P^* \approx 167$ and, with $k_l = 1/2$, $t_{\mathrm{VS}}^* \approx 25$. In our experiments and simulations, we found that velocity fluctuations grew on a timescale corresponding to $t^* \sim 25$–$50$. Based on these estimates, we find that the growth of concentration fluctuations from the lateral drift corresponding to the induced mean flow (described by Vishnampet and Saintillan) provides a reasonable prediction for our results. However, both mechanisms driving particle aggregation likely play a role in our settling suspensions.

Finally, we return to the case of a cross sheared suspension in a viscoelastic fluid. For a single particle in a cross sheared elastic fluid, the drag on a particle is significantly enhanced as a function of the shear Weissenberg number [33,41,59–61]. It has been suggested that this is due to the added tension to fluid streamlines in the shear flow direction [67] and a break in the symmetry due to a shear flow alone resulting in an increase in the viscous drag [33]. At higher Wi, regions of high polymer tension stretch out from the particle surface and modify the flow past the particle, resulting in a further drag increase [41]. This reduction of the particle settling rate is an elastic effect. In both our experiments and simulations, the mean settling rate of the suspension was below that predicted for a single particle in the same cross shear flow. We propose that this additional reduction in the settling rate is due to a homogenized suspension microstructure. The cross shear advects particles into the flow direction, and at the values of Wi tested in this work, prevents the aggregation of particle clusters as observed in the quiescent suspensions. In addition to the advection of particles, the shear flow adds a shear-induced diffusive behavior due to hydrodynamic interactions between particles [66]. We propose that these effects combine to maintain a homogeneous suspension microstructure, resulting in an overall hindered settling process. This hindrance is a finite volume fraction effect. In our experiments and simulations, we were unable to definitively identify a combined, synergistic effect of both the fluid elasticity and the finite volume fraction of the suspension. It is possible that at higher values of $\Theta_1$ and Wi, where the viscoelastic wake structures surrounding sedimenting particles become more pronounced [41], a synergistic effect could be present, as suggested by Krishnan *et al.* [27].

## VIII. CONCLUDING REMARKS

In this work, we studied the settling behavior of a suspension of rigid spherical particles in a Newtonian and viscoelastic fluid. We used both particle tracking experiments and large-scale, particle-resolved, 3D numerical simulations. In the Newtonian fluid, hindered settling (i.e., a mean settling rate less than that for a single particle) was observed with significant velocity fluctuations that decayed following random mixing, in agreement with prior studies [4]. In both experiments and simulations, the suspension structure remained homogeneous. In the viscoelastic fluid, an enhanced mean settling rate was measured relative to the Newtonian case and, in experiments, relative to a single particle. From particle tracking experiments, this enhanced mean settling rate appeared to be driven by large clusters of particles and streamers that settled quickly out of suspension. This was supported qualitatively by particle-resolved simulations, which showed evidence of the formation of fast-settling particle-rich regions that grew in intensity following random mixing. In this work, we also studied the effect of a cross shear flow on the settling behavior of a suspension of particles in a viscoelastic fluid. From both experiments and simulations, we observed a drastically hindered settling rate relative to the quiescent case. We propose that this result is due to both the effect of elasticity in a cross sheared viscoelastic fluid and the mixing of the suspension structure due to the shear flow.

This work highlights the opportunity and importance for continued study of the dynamics of a suspension of particles settling in polymeric fluids. We propose a few specific areas that deserve further investigation. First, the simulations presented in this study were unable to quantitatively predict certain experimental details—which we suggest was primarily due to a limited computational box size. As improved computational capabilities become available, this topic would benefit from a study of the effect of computational box size—both in the lateral and vertical directions—as well as box boundary conditions on the settling dynamics of particles in viscoelastic fluids. As the computational box size grows in the horizontal plane, it may also be necessary to simulate the bottom boundary of the box, as has been found for suspensions in Newtonian fluids [68,69]. Second, this study has investigated a few select points in a multi-dimensional parameter space. For the rational design of such suspensions of particles in polymeric fluids, a parametric study that maps a range of sedimentation Weissenberg number, shear Weissenberg number, and particle volume fraction could produce a phase diagram of great value. This phase diagram may help distinguish regions that produce either a stable and homogeneous or unstable and inhomogeneous settling process, revealing a set of critical conditions for suspension stability. An investigation of the effects of fluid inertia, which has been shown to qualitatively effect the settling behavior of spheres and fibers in Newtonian fluids [4,62], would also be of value. Finally, depending on the flow field, flow strength, and fluid properties, particle migration and aggregation are known to occur for nonsettling suspensions in viscoelastic fluids [1]. These effects, with respect to suspension settling behavior, deserve further investigation, and may become important to consider, for example, during mixing or in pressure-driven flows such as pipe flow or fluidization processes.

## ACKNOWLEDGMENTS

This material is based upon work supported by the National Science Foundation under Grants No. DGE-114747 (W.L.M.), No. CBET-1337051, and No. CBET-1803765; the Stanford Natural

Gas Initiative (NGI); the U.S. Army High Performance Computing Research Center (AHPCRC); and support from Stanford's High Performance Computing Center (HPCC), including use of the Certainty and Shephard computing clusters. Part of this work was performed at the Stanford Nano Shared Facilities (SNSF), supported by the National Science Foundation under Award No. ECCS-1542152. The authors thank Dr. Sreenath Krishnan and Prof. Gianluca Iaccarino for their helpful and insightful suggestions on the suspension simulations.

---

[1] G. D'Avino and P. L. Maffettone, Particle dynamics in viscoelastic liquids, J. Non-Newtonian Fluid Mech. **215**, 80 (2015).

[2] R. Zenit and J. J. Feng, Hydrodynamic interactions among bubbles, drops, and particles in non-Newtonian liquids, Ann. Rev. Fluid Mech. **50**, 505 (2018).

[3] R. H. Davis and A. Acrivos, Sedimentation of noncolloidal particles at low Reynolds numbers, Annu. Rev. Fluid Mech. **17**, 91 (1985).

[4] É. Guazzelli and J. Hinch, Fluctuations and instability in sedimentation, Annu. Rev. Fluid Mech. **43**, 97 (2011).

[5] G. K. Batchelor, Sedimentation in a dilute dispersion of spheres, J. Fluid Mech. **52**, 245 (1972).

[6] E. Allen and P. H. T. Uhlherr, Nonhomogeneous sedimentation in viscoelastic fluids, J. Rheol. **33**, 627 (1989).

[7] S. Bobroff and R. J. Phillips, Nuclear magnetic resonance imaging investigation of sedimentation of concentrated suspensions in non-Newtonian fluids, J. Rheol. **42**, 1419 (1998).

[8] S. Daugan, L. Talini, B. Herzhaft, Y. Peysson, and C. Allain, Sedimentation of suspensions in shear-thinning fluids, Oil Gas Sci. Technol. Rev. IFP **59**, 71 (2004).

[9] S. Mora, L. Talini, and C. Allain, Structuring Sedimentation in a Shear-Thinning Fluid, Phys. Rev. Lett. **95**, 088301 (2005).

[10] D. D. Joseph, Y. J. Liu, M. Poletto, and J. Feng, Aggregation and dispersion of spheres falling in viscoelastic liquids, J. Non-Newtonian Fluid Mech. **54**, 45 (1994).

[11] R. J. Phillips, Structural instability in the sedimentation of particulate suspensions through viscoelastic fluids, J. Non-Newtonian Fluid Mech. **165**, 479 (2010).

[12] R. Vishnampet and D. Saintillan, Concentration instability of sedimenting spheres in a second-order fluid, Phys. Fluids **24**, 073302 (2012).

[13] P. Brunn, The slow motion of a sphere in a second-order fluid, Rheol. Acta **15**, 163 (1976); **16**, 324 (1977).

[14] J. Einarsson and B. Mehlig, Spherical particle sedimenting in weakly viscoelastic shear flow, Phys. Rev. Fluids **2**, 063301 (2017).

[15] A. Zhang, W. L. Murch, J. Einarsson, and E. S. G. Shaqfeh, Lift and drag force on a spherical particle in a viscoelastic shear flow, J. Non-Newtonian Fluid Mech. **280**, 104279 (2020).

[16] D. L. Koch and E. S. G. Shaqfeh, The instability of a dispersion of sedimenting spheroids, J. Fluid Mech. **209**, 521 (1989).

[17] D. Saintillan, E. S. G. Shaqfeh, and E. Darve, The growth of concentration fluctuations in dilute dispersions of orientable and deformable particles under sedimentation, J. Fluid Mech. **553**, 347 (2006).

[18] P. Singh, D. D. Joseph, T. I. Hesla, R. Glowinski, and T.-W. Pan, A distributed Lagrange multiplier/fictitious domain method for viscoelastic particulate flows, J. Non-Newtonian Fluid Mech. **91**, 165 (2000).

[19] Z. Yu, N. Phan-Thien, Y. Fan, and R. I. Tanner, Viscoelastic mobility problem of a system of particles, J. Non-Newtonian Fluid Mech. **104**, 87 (2002).

[20] R. J. Phillips and L. Talini, Chaining of weakly interacting particles suspended in viscoelastic fluids, J. Non-Newtonian Fluid Mech. **147**, 175 (2007).

[21] J. Hao, T.-W. Pan, R. Glowinski, and D. D. Joseph, A fictitious domain/distributed Lagrange multiplier method for the particulate flow of Oldroyd-B fluids: A positive definiteness preserving approach, J. Non-Newtonian Fluid Mech. **156**, 95 (2009).

[22] T.-W. Pan and R. Glowinski, On the dynamics of particle sedimentation in viscoelastic fluids: A numerical study on particle chaining in two-dimensional narrow channels, J. Non Newtonian Fluid Mech. **244**, 44 (2017).

[23] Z. Yu, A. Wachs, and Y. Peysson, Numerical simulation of particle sedimentation in shear-thinning fluids with a fictitious domain method, J. Non Newtonian Fluid Mech. **136**, 126 (2006).

[24] A. Decoene, S. Martin, and B. Maury, Direct simulation of rigid particles in a viscoelastic fluid, J. Non-Newtonian Fluid Mech. **260**, 1 (2018).

[25] T.-W. Pan and R. Glowinski, Numerical study of spheres settling in Oldroyd-B fluids, Phys. Fluids **30**, 113102 (2018).

[26] N. Goyal and J. J. Derksen, Direct simulations of spherical particles sedimenting in viscoelastic fluids, J. Non Newtonian Fluid Mech. **183-184**, 1 (2012).

[27] S. Krishnan, E. S. G. Shaqfeh, and G. Iaccarino, Fully resolved viscoelastic particulate simulations using unstructured grids, J. Comput. Phys. **338**, 313 (2017).

[28] M. Yang and E. S. G. Shaqfeh, Mechanism of shear thickening in suspensions of rigid spheres in Boger fluids. Part II: Suspensions at finite concentration, J. Rheol. **62**, 1379 (2018).

[29] D. Alghalibi, I. Lashgari, L. Brandt, and S. Hormozi, Interface-resolved simulations of particle suspensions in Newtonian, shear thinning and shear thickening carrier fluids, J. Fluid Mech. **852**, 329 (2018).

[30] C. Fernandes, S. A. Faroughi, O. S. Carneiro, J. M. Nóbrega, and G. H. McKinley, Fully resolved simulations of particle-laden viscoelastic fluids using an immersed boundary method, J. Non-Newtonian Fluid Mech. **266**, 80 (2019).

[31] A. C. Barbati, J. Descroches, A. Robisson, and G. H. McKinley, Complex fluids and hydraulic fracturing, Annu. Rev. Chem. Biomol. Eng. **7**, 415 (2016).

[32] N. Tonmukayakul, J. F. Morris, and R. Prud'homme, Method for estimating proppant transport and suspendability of viscoelastic liquids, U.S. Patent No. 8,424,368 (2013).

[33] S. Padhy, E. S. G. Shaqfeh, G. Iaccarino, J. F. Morris, and N. Tonmukayakul, Simulations of a sphere sedimenting in a viscoelastic fluid with cross shear flow, J. Non-Newtonian Fluid Mech. **197**, 48 (2013).

[34] A. V. Bazilevskii, D. A. Koroteev, A. N. Rozhkov, and A. A. Skobeleva, Sedimentation of particles in shear flows of viscoelastic fluids, Fluid Dyn. **45**, 626 (2010).

[35] J. M. Ham and G. M. Homsy, Hindered settling and hydrodynamic dispersion in quiescent sedimenting suspensions, Int. J. Multiphase Flow **14**, 533 (1988).

[36] H. Nicolai, B. Herzhaft, E. J. Hinch, L. Oger, and É. Guazzelli, Particle velocity fluctuations and hydrodynamic self-diffusion of sedimenting non-Brownian spheres, Phys. Fluids **7**, 12 (1995).

[37] D. V. Boger, A highly elastic constant-viscosity fluid, J. Non-Newtonian Fluid Mech. **3**, 87 (1977).

[38] D. V. Boger and H. Nguyen, A model viscoelastic fluid, Polym. Eng. Sci. **18**, 1037 (1978).

[39] R. J. Binnington and D. V. Boger, Constant viscosity elastic liquids, J. Rheol. **29**, 887 (1985).

[40] D. F. James, Boger fluids, Annu. Rev. Fluid Mech. **41**, 129 (2009).

[41] W. L. Murch, S. Krishnan, E. S. G. Shaqfeh, and G. Iaccarino, Growth of viscoelastic wings and the reduction of particle mobility in a viscoelastic shear flow, Phys. Rev. Fluids **2**, 103302 (2017).

[42] R. B. Bird, R. C. Armstrong, and O. Hassager, *Dynamics of Polymeric Liquids*, 2nd ed., Vol. 1: Fluid Mechanics (Wiley-Interscience, Hoboken, NJ, 1987).

[43] R. B. Bird, C. F. Curtiss, R. C. Armstrong, and O. Hassager, *Dynamics of Polymeric Liquids*, 2nd ed., Vol. 2: Kinetic Theory (Wiley-Interscience, Hoboken, NJ, 1987).

[44] G. D'Avino, F. Snijkers, R. Pasquino, M. A. Hulsen, F. Greco, P. L. Maffettone, and J. Vermant, Migration of a sphere suspended in viscoelastic liquids in Couette flow: Experiments and simulations, Rheol. Acta **51**, 215 (2012).

[45] C. A. Schneider, W. S. Rasband, and K. W. Eliceiri, NIH image to ImageJ: 25 years of image analysis, Nat. Methods **9**, 671 (2012).

[46] C. T. Rueden, J. Schindelin, M. C. Hiner, B. E. DeZonia, A. E. Walter, E. T. Arena, and K. W. Eliceiri, ImageJ2: ImageJ for the next generation of scientific image data, BMC bioinformatics **18**, 529 (2017).

[47] J. Schindelin, I. Arganda-Carreras, E. Frise, V. Kaynig, M. Longair, T. Pietzsch, S. Preibisch, C. Rueden, S. Saalfeld, B. Schmid, J.-Y. Tinevez, D. J. White, V. Hartenstein, K. Eliceiri, P. Tomancak, and A. Cardona, Fiji: An open-source platform for biological-image analysis, Nat. Methods **9**, 676 (2012).

[48] J.-Y. Tinevez, N. Perry, J. Schindelin, G. M. Hoopes, G. D. Reynolds, E. Laplantine, S. Y. Bednarek, S. L. Shorte, and K. W. Eliceiri, TrackMate: An open and extensible platform for single-particle tracking, Methods **115**, 80 (2017).

[49] D. Richter, G. Iaccarino, and E. S. G. Shaqfeh, Simulations of three-dimensional viscoelastic flows past a circular cylinder at moderate Reynolds numbers, J. Fluid Mech. **651**, 415 (2010).

[50] M. Bajaj, M. Pasquali, and J. R. Prakash, Coil-stretch transition and the breakdown of computations for viscoelastic fluid flow around a confined cylinder, J. Rheol. **52**, 197 (2008).

[51] B. Yang and B. Khomami, Simulations of sedimentation of a sphere in a viscoelastic fluid using molecular based constitutive models, J. Non-Newtonian Fluid Mech. **82**, 429 (1999).

[52] R. Glowinski, T.-W. Pan, T. I. Hesla, D. D. Joseph, and J. Periaux, A fictitious domain approach to the direct numerical simulation of incompressible viscous flow past moving rigid bodies: Application to particulate flow, J. Comput. Phys. **169**, 363 (2001).

[53] H. H. Hu, N. A. Patankar, and M. Y. Zhu, Direct numerical simulations of fluid–solid systems using the arbitrary Lagrangian–Eulerian technique, J. Comput. Phys. **169**, 427 (2001).

[54] H. Faxén, Der widerstand gegen die bewegung einer starren kugel in einer zähen flüssigkeit, die zwischen zwei parallelen ebenen wänden eingeschlossen ist, Ann. Phys. **373**, 89 (1922).

[55] R. P. Chhabra, *Bubbles, Drops, and Particles in Non-Newtonian Fluids*, 2nd ed. (CRC Press, Boca Raton, 2006), Chap. 5.

[56] G. H. McKinley, Steady and transient motion of spherical particles in viscoelastic liquids, in *Transport Processes in Bubbles, Drops and Particles*, 2nd ed., edited by D. De Kee and R. P. Chhabra (CRC Press, Boca Raton, 2002), Chap. 14, pp. 338–375.

[57] See Supplemental Material at http://link.aps.org/supplemental/10.1103/PhysRevFluids.5.073301 for a movie showing the static sedimentation experiments.

[58] É. Guazzelli, Evolution of particle-velocity correlations in sedimentation, Phys. Fluids **13**, 1537 (2001).

[59] B. H. A. A. van den Brule and G. Gheissary, Effects of fluids elasticity on the static and dynamic settling of a spherical particle, J. Non-Newtonian Fluid Mech. **49**, 123 (1993).

[60] K. D. Housiadas and R. I. Tanner, The drag of a freely sedimentating sphere in a sheared weakly viscoelastic fluid, J. Non-Newtonian Fluid Mech. **183–184**, 52 (2012).

[61] S. Padhy, M. Rodriguez, E. S. G. Shaqfeh, G. Iaccarino, J. F. Morris, and N. Tonmukayakul, The effect of shear thinning and walls on the sedimentation of a sphere in an elastic fluid under orthogonal shear, J. Non-Newtonian Fluid Mech. **201**, 120 (2013).

[62] E. J. Hinch, Sedimentation of small particles, in *Disorder and Mixing* (Springer, Berlin, 1988), pp. 153–162.

[63] É. Guazzelli and J. F. Morris, *A Physical Introduction to Suspension Dynamics* (Cambridge University Press, Cambridge, 2011), Chap. 6.

[64] L. Bergougnoux and É. Guazzelli, Non-Poisson statistics of settling spheres, Phys. Fluids **21**, 091701 (2009).

[65] D. D. Joseph and J. Feng, A note on the forces that move particles in a second-order fluid, J. Non-Newtonian Fluid Mech. **64**, 299 (1996).

[66] R. H. Davis, Hydrodynamic diffusion of suspended particles: A symposium, J. Fluid Mech. **310**, 325 (1996).

[67] R. I. Tanner, K. D. Housiadas, and F. Qi, Mechanism of drag increase on spheres in viscoelastic cross-shear flows, J. Non-Newtonian Fluid Mech. **203**, 51 (2014).

[68] A. J. C. Ladd, Effects of container walls on the velocity fluctuations of sedimenting spheres, Phys. Rev. Lett. **88**, 048301 (2002).

[69] N.-Q. Nguyen and A. J. C. Ladd, Sedimentation of hard-sphere suspensions at low Reynolds number, J. Fluid Mech. **525**, 73 (2005).